Available online at www.sciencedirect.com
ScienceDirect
Comput. Methods Appl. Mech. Engrg. 373 (2021) 113451
Computer methods in applied mechanics and engineering
www.elsevier.com/locate/cma

High-order finite element methods for a pressure Poisson equation reformulation of the Navier–Stokes equations with electric boundary conditions

Rodolfo Ruben Rosales[a], Benjamin Seibold[b], David Shirokoff[c,*], Dong Zhou[d]

[a] *Department of Mathematics, Massachusetts Institute of Technology, 77 Massachusetts Avenue, Cambridge, MA 02139, United States of America*
[b] *Department of Mathematics, Temple University, 1805 North Broad Street, Philadelphia, PA 19122, United States of America*
[c] *Department of Mathematical Sciences, New Jersey Institute of Technology, University Heights, Newark, NJ 07102, United States of America*
[d] *Department of Mathematics, California State University, Los Angeles, 5151 State University Drive, Los Angeles, CA 90032, United States of America*

Received 22 February 2020; received in revised form 10 August 2020; accepted 17 September 2020
Available online xxxx

Abstract

Pressure Poisson equation (PPE) reformulations of the incompressible Navier–Stokes equations (NSE) replace the incompressibility constraint by a Poisson equation for the pressure and a suitable choice of boundary conditions. This yields a time-evolution equation for the velocity field only, with the pressure gradient acting as a nonlocal operator. Thus, numerical methods based on PPE reformulations are representatives of a class of methods that have no principal limitations in achieving high order. In this paper, it is studied to what extent high-order methods for the NSE can be obtained from a specific PPE reformulation with electric boundary conditions (EBC). To that end, implicit–explicit (IMEX) time-stepping is used to decouple the pressure solve from the velocity update, while avoiding a parabolic time-step restriction; and mixed finite elements are used in space, to capture the structure imposed by the EBC. Via numerical examples, it is demonstrated that the methodology can yield at least third order accuracy in space and time.

MSC: 65L06; 65M60; 76D05

Keywords: Incompressible Navier–Stokes; Pressure Poisson equation; Electric boundary conditions; Mixed finite elements; IMEX schemes

1. Introduction

Developing efficient high-order time stepping methods for the incompressible Navier–Stokes equations (NSE) is challenging due to the fact that the velocity and pressure are coupled via an incompressibility constraint. Numerical methods that treat both the velocity $\boldsymbol{u}$ and the pressure p in an implicit fashion [1] provide a comparatively straightforward pathway towards high-order. However, approaches that are implicit in both $\boldsymbol{u}$ and p result in large (possibly nonlinear) saddle-point systems. This imposes a requirement to select spatial discretizations that ensure

* Corresponding author.
E-mail addresses: rrr@math.mit.edu (R.R. Rosales), seibold@temple.edu (B. Seibold), david.g.shirokoff@njit.edu (D. Shirokoff), dong.zhou@calstatela.edu (D. Zhou).
URLs: http://www.math.temple.edu/~seibold (B. Seibold), http://web.njit.edu/~shirokof (D. Shirokoff).

https://doi.org/10.1016/j.cma.2020.113451

stable solutions of the resulting discrete equations (i.e. staggered grids [2], or finite elements satisfying the inf–sup condition [3]). In addition, the resulting discrete saddle point problems are sometimes non-trivial to solve efficiently [4,5]. Improvements to preconditioning and multigrid methods (see, for instance, [6,7] for applications to the linearized Navier–Stokes/Oseen equation, and [8–11] for the Stokes equation), as well as finite element spaces (see [12,13]), have led to more robust and faster fully implicit schemes. For instance, highly accurate benchmark tests and large eddy simulations [14,15], as well as finite element libraries such as Deal.II [16,17] implement and solve schemes implicit in both $(\boldsymbol{u}, p)$. Nevertheless, due to the broad importance of the NSE, possible software/legacy constraints, as well as fundamental mathematical interest, alternative approaches that are not implicit in both $(\boldsymbol{u}, p)$ remain of interest.

Many numerical approaches that decouple $\boldsymbol{u}$ and p result in smaller systems of equations with fewer coupled variables, and often times avoid a saddle-point structure. Hence, such methodologies are attractive for certain large-scale problems. Historically, it has been challenging to achieve high-order in time when decoupling velocity and pressure, particularly in a unified systematic fashion; and only recently such methodologies have been introduced. This paper develops finite element approaches for certain pressure Poisson equation (PPE) reformulations of the Navier–Stokes equations that allow for a systematic pathway towards high order while decoupling velocity and pressure. We also stress that there is a merit in presenting such methods, as not every existing Navier–Stokes equations framework is compatible with using recently developed saddle-point solvers.

Numerical methods for the NSE that decouple velocity and pressure date back to the late 1960s with the introduction of projection methods [18,19]. The idea of projection methods is to first evolve the velocity without the pressure, and then project the velocity back into the space of divergence-free fields via a Poisson problem. Projection methods are one example of a larger class of methods known as fractional step methods [20]. Efforts have been made in the past few decades to improve the accuracy of projection and fractional step methods to second order (in time), and higher, [21–24]. In particular, accurate methods that go beyond second order are an ongoing area of research [25,26]. In addition to the difficulties of achieving high order in time accuracy, projection methods carry the risk of producing numerical boundary layers via the Poisson equation for the pressure, which causes a degradation in spatial error convergence. An extensive overview of projection methods is given by Guermond, Minev, and Shen in [27], where projection methods and various improvements, as well as their theoretical and numerical convergence results are discussed. Despite the difficulties, recent work [28,29] has devised projection methods with deferred correction time-stepping demonstrating up to 8th, respectively 12th, order in time (in the absence of order reduction effects). Lastly, recent progress on generalizing the artificial compressibility method [30,31] (which has traditionally been first order in time) has lead to alternative avenues that obtain high-order (beyond second order) in time schemes.

PPE reformulations of the Navier–Stokes equations [32–45] provide an alternate route towards devising high-order in time numerical methods. The basic idea underlying PPE approaches is not to discretize the NSE directly, but instead to (i) reformulate the NSE into a system of PDEs with a Poisson equation for the pressure in lieu of the divergence constraint (the PPE system), (ii) devise boundary conditions that ensure that the new set of equations guarantees incompressibility [22,32,33,41], and then (iii) discretize and solve the resulting PPE system. The solution to the Poisson equation for the pressure is designed so that the PPE reformulation is equivalent to the original NSE for solutions that are sufficiently smooth. In other words, at the continuous level, solving the PPE is equivalent to solving the Navier–Stokes equations. In a sequence of work by Henshaw et al. [33–35,46], the recovery of the pressure through the solution of a pressure Poisson problem was done in a discrete setting (with finite differences), using the boundary condition $\nabla \cdot \boldsymbol{u} = 0$ together with other numerical boundary conditions. PPE formulations as PDEs were introduced in [38] by Johnston and Liu, and in [42] by Shirokoff and Rosales. Once the PPE has been formulated as a set of continuous PDEs, one may then examine a variety of different numerical discretizations (in both space and time) to solve the PPE system (and hence, equivalently, the NSE).

One important advantage of PPE reformulations compared to the standard form of the NSE is that by solving the Poisson equation, the pressure can be viewed as a global function of the velocity field $p = P(\boldsymbol{u})$. The fact that the pressure can be written as a function of the velocity enables straightforward numerical approaches for decoupling the velocity and pressure, i.e. to enable implicit–explicit time-stepping strategies. PPE reformulations then provide the possibility to devise high-order in time numerical methods within a systematic framework. Note also that (unlike the NSE) PPE reformulations are defined even if the initial conditions are not incompressible [42,47], which can be an important advantage when dealing with real data. Drawbacks of PPE reformulations are: (i) For the numerical

solution, the (numerical) divergence field may not always be exactly zero. (ii) The pressure boundary conditions are typically complicated. Thus their interaction with the velocity is not straightforward to understand and analyze.

Here we focus on numerical methods based on the Shirokoff–Rosales (SR) PPE reformulation proposed in [42]. Numerical discretizations for the SR PPE reformulation have been proposed in the context of standard finite difference methods [42] and meshfree finite difference method [48]. In [42], a second order finite difference scheme was proposed using a staggered spatial grid and a second order semi-implicit strategy in time where the viscous term was treated implicitly via Crank–Nicolson and the pressure was treated explicitly using a second order Adams–Bashforth method. Curved boundaries were embedded into a Cartesian grid, which could successfully handle irregular domains, but it was cumbersome to implement and did not generalize to arbitrary order. Meshfree finite difference methods for the SR PPE reformulation were devised in [48] as an alternative to allow for the handling of irregular domains (without re-entrant corners). Specifically, [48] devised second order schemes with implicit–explicit time-stepping. Extensions to higher spatial order require larger stencils, thus lead to denser matrices and more costly computations.

In this paper we investigate a finite element discretization for a PPE reformulation with electric boundary conditions motivated by the SR PPE. The approach has the advantage of allowing for a systematic extension to higher spatial order. We also use implicit–explicit (IMEX) time-stepping, specifically IMEX Runge–Kutta (RK) methods that decouple the velocity and the pressure solves. We study the extent to which this yields desirable convergence and stability properties — i.e. better than second order in time, while avoiding a parabolic time step restriction $\Delta t = O(\Delta x^2)$. As a final note, we remark that the global existence of weak solutions to the SR PPE reformulation, as well as to the Johnston and Liu [38] PPE reformulation, has been proved [47] for no-slip boundary conditions. The proofs provide appropriate function spaces for the weak solutions, but they do not pursue finite element discretizations of the weak solutions.

This paper is organized as follows. In Section 2, we introduce a PPE reformulation motivated by the SR PPE of the Navier–Stokes equations. This reformulation uses non-standard boundary conditions for the velocity — i.e. electric boundary conditions (EBC). The resulting vector Poisson-type problem with EBC, when solved with standard nodal FEM, exhibits the Babuška paradox, which can be overcome by using a mixed FEM formulation. In Section 3, we present a numerical method for the *linear* time-dependent problem (i.e. without the nonlinear advection term), based on mixed FEM and IMEX RK time-stepping. We illustrate, via numerical tests, that the proposed method can achieve (at least) 3rd order in space and in time. In Section 4, we discuss how to extend the proposed method to the nonlinear case. Numerical results are shown, for manufactured solutions in 2D and 3D, as well as for practical benchmark examples (lid-driven cavity, backward-facing step).

2. Pressure Poisson equation reformulation of the Navier–Stokes equations

In this section, we introduce a pressure Poisson equation reformulation of the Navier–Stokes equations with electric boundary conditions similar to the one proposed in [42]. Consider the time-dependent incompressible Navier–Stokes equations (NSE) in a connected domain $\Omega \in \mathbb{R}^N$, where $N = 2$ or 3, with a piece-wise smooth boundary $\partial\Omega$, for domains with Dirichlet boundary data,

$$\boldsymbol{u}_t + (\boldsymbol{u}\cdot\nabla)\boldsymbol{u} = \nu\Delta\boldsymbol{u} - \nabla p + \boldsymbol{f} \quad \text{in } \Omega\times(0,T], \tag{2.1a}$$

$$\nabla\cdot\boldsymbol{u} = 0 \quad \text{in } \Omega\times(0,T], \tag{2.1b}$$

$$\boldsymbol{u}(\boldsymbol{x},t) = \boldsymbol{g}(\boldsymbol{x},t) \quad \text{on } \partial\Omega\times[0,T], \tag{2.1c}$$

$$\boldsymbol{u}(\boldsymbol{x},0) = \boldsymbol{u}_0(\boldsymbol{x}) \quad \text{in } \Omega, \tag{2.1d}$$

where $\nu > 0$ is the kinematic viscosity. Eq. (2.1a) follows from the conservation of momentum, and (2.1b) is conservation of mass. Furthermore, we impose the following compatibility conditions:

$$\text{Continuity between the initial and the boundary conditions: } \boldsymbol{u}_0(\boldsymbol{x}) = \boldsymbol{g}(\boldsymbol{x},0) \text{ on } \partial\Omega. \tag{2.2}$$

$$\text{Incompressibility of the initial condition: } \nabla\cdot\boldsymbol{u}_0 = 0 \text{ in } \Omega. \tag{2.3}$$

$$\text{Zero net flux through the boundary: } \int_{\partial\Omega} \boldsymbol{n}\cdot\boldsymbol{g}\ \mathrm{d}S = 0. \tag{2.4}$$

For the numerical solution of (2.1) we will instead solve a PPE reformulation, whose fundamental difference from previously proposed PPE reformulations lies in the velocity boundary conditions: incompressibility and the

tangential flow are prescribed at the boundary. Further, the normal velocity is enforced via a relaxation term in the pressure equation. The PPE reformulation reads as follows

$$\boldsymbol{u}_t + (\boldsymbol{u}\cdot\nabla)\boldsymbol{u} = \nu\Delta\boldsymbol{u} - \nabla P(\boldsymbol{u}) + \boldsymbol{f} \quad \text{in } \Omega\times(0,T], \tag{2.5a}$$

$$\boldsymbol{n}\times\boldsymbol{u} = \boldsymbol{n}\times\boldsymbol{g} \quad \text{on } \partial\Omega\times[0,T], \tag{2.5b}$$

$$\nabla\cdot\boldsymbol{u} = 0 \quad \text{on } \partial\Omega\times[0,T]. \tag{2.5c}$$

Here $P(\boldsymbol{u})$ is the solution to the pressure Poisson equation:

$$\Delta p = \nabla\cdot(\boldsymbol{f} - (\boldsymbol{u}\cdot\nabla)\boldsymbol{u}) \quad \text{in } \Omega, \tag{2.6a}$$

$$\frac{\partial p}{\partial \boldsymbol{n}} = \boldsymbol{n}\cdot\left(\boldsymbol{f} - \boldsymbol{g}_t - \nu\nabla\times\nabla\times\boldsymbol{u} - (\boldsymbol{u}\cdot\nabla)\boldsymbol{u}\right) + \lambda\boldsymbol{n}\cdot(\boldsymbol{u}-\boldsymbol{g}) \quad \text{on } \partial\Omega. \tag{2.6b}$$

Note that two notations are used for the pressure: p to denote the field quantity, and $P(\boldsymbol{u})$ to denote the fact that (2.6) defines the pressure as a function of the velocity $\boldsymbol{u}$, i.e. $p = P(\boldsymbol{u})$. Note that the operator P also depends on the normal boundary data $\boldsymbol{n}\cdot\boldsymbol{g}$ and the forcing $\boldsymbol{f}$, through which it may be time-dependent. The term $\lambda\boldsymbol{n}\cdot(\boldsymbol{u}-\boldsymbol{g})$, where $\lambda > 0$ is a constant, is a relaxation term that guarantees that the normal velocity condition at the boundary $\partial\Omega$ is exponentially attracting — see Eq. (2.8).

The tangential boundary conditions, together with the divergence-free boundary condition in (2.5), often appear in electrostatics as "electric boundary conditions" (EBC). We adopt this terminology in this paper. The PPE system (2.5)–(2.6) is almost identical to the one introduced in [42], the difference being here that $\boldsymbol{n}\cdot\nabla\times\nabla\times\boldsymbol{u}$ appears in the boundary condition for p in lieu of $\boldsymbol{n}\cdot\Delta\boldsymbol{u}$ (which appeared in [42]). The choice of $\boldsymbol{n}\cdot\nabla\times\nabla\times\boldsymbol{u}$ in the pressure boundary condition is done to yield a simpler finite element discretization for the pressure than $\boldsymbol{n}\cdot\Delta\boldsymbol{u}$. Note that the pressure boundary condition $\boldsymbol{n}\cdot\nabla\times\nabla\times\boldsymbol{u}$ has appeared in several projection method and PPE formulations with Dirichlet boundary conditions for the velocity such as [22,26,38]. We re-emphasize that our goal is to examine PPE schemes with EBC in the velocity.

2.1. Equivalence of the PPE system with Navier–Stokes for strong solutions

In previous works, the PPE systems in [42] and [38] were shown to be, for sufficiently smooth (up to the boundary) solutions $(\boldsymbol{u}, p)$, equivalent to the NSE (2.1). It is relatively straightforward to show that smooth solutions to the NSE solve (2.5)–(2.6) and hence the PPE system contains the NSE solutions. We now show that solutions to the PPE system (2.5)–(2.6) solve the NSE — the approach follows closely to [38,42] with a minor difference due to the combination of the EBC for the velocity and $\boldsymbol{n}\cdot\nabla\times\nabla\times\boldsymbol{u}$ boundary condition for the pressure.

Assume that $(\boldsymbol{u}, p)$ is a smooth solution to (2.5)–(2.6). Then the PPE reformulation recovers the incompressibility constraint: apply the divergence to the momentum equation (2.5a) and substitute into (2.6a). This yields the heat equation for the divergence $\phi = \nabla\cdot\boldsymbol{u}$, with homogeneous Dirichlet boundary conditions due to (2.5c). That is:

$$\begin{cases} \phi_t = \nu\Delta\phi & \text{in } \Omega, \\ \phi = 0 & \text{on } \partial\Omega. \end{cases} \tag{2.7}$$

Therefore, if $\phi(t=0) = \nabla\cdot\boldsymbol{u}_0 = 0$, then $\phi = 0$ for all time, and $\boldsymbol{u}$ is incompressible. If, due to numerical approximation errors, the velocity field starts to depart from the $\nabla\cdot\boldsymbol{u} = 0$ subspace, the heat equation dynamics ensure that $\boldsymbol{u}$ is driven back towards incompressibility. This property indicates that there is no need to impose a discrete incompressibility principle in PPE reformulations, thus providing more flexibility in the design of numerical approximation methods.

Secondly, the PPE ensures that the normal velocity at the boundary, i.e. $\boldsymbol{n}\cdot\boldsymbol{u} = \boldsymbol{n}\cdot\boldsymbol{g}$, is enforced implicitly through the ordinary differential equation

$$\begin{cases} \boldsymbol{n}\cdot(\boldsymbol{u}_t - \boldsymbol{g}_t) = \nu\boldsymbol{n}\cdot\nabla\phi - \lambda\boldsymbol{n}\cdot(\boldsymbol{u}-\boldsymbol{g}) & \text{on } \partial\Omega\times(0,T], \\ \boldsymbol{n}\cdot(\boldsymbol{u}-\boldsymbol{g})|_{\partial\Omega} = 0 & \text{at } t = 0, \end{cases} \tag{2.8}$$

which is obtained by evaluating the normal component of the momentum equation (2.5a) at the boundary, and using the pressure boundary condition (2.6b) along with the identity that $\Delta\boldsymbol{u} = \nabla(\nabla\cdot\boldsymbol{u}) - \nabla\times\nabla\times\boldsymbol{u}$. By virtue of Eq. (2.7), we have that $\phi = 0$, so that (2.8) reduces to a simple ODE at every point $\boldsymbol{x}\in\partial\Omega$: $\dot{\alpha} = -\lambda\alpha$ where $\alpha = \boldsymbol{n}\cdot(\boldsymbol{u}-\boldsymbol{g})$. Hence, $\boldsymbol{n}\cdot\boldsymbol{u} = \boldsymbol{n}\cdot\boldsymbol{g}$ for all time.

Remark 2.1 (*Solvability Condition for the Pressure Poisson Equation*)**.** A solvability condition is required in order for the pressure Poisson equation (2.6) to have a solution, that is:

$$\int_{\Omega} -\nu\nabla\cdot(\nabla\times\nabla\times\boldsymbol{u})+\lambda\nabla\cdot\boldsymbol{u}\ \mathrm{d}V-\int_{\partial\Omega}\boldsymbol{n}\cdot\boldsymbol{g}_t+\lambda\boldsymbol{n}\cdot\boldsymbol{g}\ \mathrm{d}S=0. \tag{2.9}$$

The incompressibility condition $\nabla\cdot\boldsymbol{u}=0$ and the zero net flux condition (2.4) ensure that both the volume integral and the boundary integral in Eq. (2.9) vanish. However, numerical approximation errors in the discrete Poisson equation may result in schemes that do not exactly satisfy the discrete version of the solvability condition (2.9). One possibility, when this occurs, is to solve the discrete Poisson equation in the least squares sense. The least squares solution is achieved by formulating an augmented system that projects the right hand side of the pressure Poisson problem onto one for which the solvability condition is satisfied, see the Appendix.

Remark 2.2. There is a rich variety of possible PPE reformulations. At the continuum level, one can add $\nabla\cdot\boldsymbol{u}$ anywhere (because $\nabla\cdot\boldsymbol{u}=0$), as long as the resulting systems are well-posed and are equivalent to the original problem. However, in the presence of approximation errors, one generally has $\nabla\cdot\boldsymbol{u}_h\neq 0$, thus adding $\nabla\cdot\boldsymbol{u}$ will lead to different numerical schemes. For example, Henshaw and Petersson [35] add a divergence damping term $\delta\,\nabla\cdot\boldsymbol{u}$, with $\delta\geq 0$, to the pressure Poisson equation to obtain

$$\Delta p=\nabla\cdot(\boldsymbol{f}-(\boldsymbol{u}\cdot\nabla)\boldsymbol{u})+\delta\nabla\cdot\boldsymbol{u}.$$

With this, the divergence satisfies the PDE $\phi_t=\Delta\phi-\delta\phi$. In the discretized case, where the divergence is not exactly zero, the damping term adds an exponential decay that can further help keeping the discrete divergence small.

3. Numerical method for the time-dependent Stokes problem

In this section, we present a numerical method for the PPE reformulation (2.5)–(2.6) of the time-dependent Stokes equation

$$\boldsymbol{u}_t=\nu\Delta\boldsymbol{u}-\nabla P(\boldsymbol{u})+\boldsymbol{f}\quad\text{ in }\Omega\times(0,T],\quad \boldsymbol{n}\times\boldsymbol{u}=\boldsymbol{n}\times\boldsymbol{g}\text{ and }\nabla\cdot\boldsymbol{u}=0\quad\text{on }\partial\Omega\times[0,T], \tag{3.1}$$

where $P(\boldsymbol{u})$ solves the pressure Poisson equation

$$\Delta p=\nabla\cdot\boldsymbol{f}\quad\text{ in }\Omega,\quad \frac{\partial p}{\partial\boldsymbol{n}}=\boldsymbol{n}\cdot(\boldsymbol{f}-\boldsymbol{g}_t-\nu\nabla\times\nabla\times\boldsymbol{u})+\lambda\boldsymbol{n}\cdot(\boldsymbol{u}-\boldsymbol{g})\quad\text{on }\partial\Omega. \tag{3.2}$$

To handle irregular domains we adopt a mixed finite element method (FEM) for the spatial discretizations of $\boldsymbol{u}$ (see Section 3.1), and nodal FEM for p (see Section 3.2). Note that the motivation for adopting a mixed FEM for $\boldsymbol{u}$ is to address structural issues (discussed below) that arise from the electric boundary conditions (EBC) in the momentum equation. Unlike mixed approaches for the Stokes/Navier–Stokes equations in which the elements approximating $\boldsymbol{u}$ and p need to satisfy a discrete inf–sup condition [3,49], the mixed formulation employed here is solely for the velocity, and the nodal elements for the pressure do not need to satisfy an inf–sup condition with the velocity elements. For the time evolution (see Section 3.3), we adopt an implicit–explicit (IMEX) Runge–Kutta (RK) scheme that (due to the PPE formulation) leads to natural approaches for decoupling the velocity $\boldsymbol{u}$ from the pressure p. That is, we treat the viscous term $\Delta\boldsymbol{u}$ implicitly and the pressure term ∇p explicitly. We carry out convergence studies via the method of manufactured solutions in Section 3.4.

3.1. Spatial discretization of the velocity via mixed finite elements

In this section we outline the spatial discretization of the velocity via mixed finite elements [3]. The choice of a mixed FEM over other element choices (such as nodal FEM) is due to the EBC in the momentum equation. To be precise, nodal FEM for problems involving electric boundary conditions may converge to the wrong solution, see Remark 3.1. In contrast, mixed FE provide a natural way to handle the EBC.

The mixed formulation presented in this paper is applied to the discretization of the momentum equation (2.5) only, and introduced to handle the EBC by introducing the vorticity $\boldsymbol{\omega}=\nabla\times\boldsymbol{u}$ as a new variable. Hence, there is no inf–sup condition for $(\boldsymbol{u},p)$, but instead, an inf–sup condition for the velocity and vorticity $(\boldsymbol{u},\boldsymbol{\omega})$. Using the

vector identity $\Delta \boldsymbol{u} = \nabla(\nabla \cdot \boldsymbol{u}) - \nabla \times \nabla \times \boldsymbol{u}$, and introducing the new variable $\boldsymbol{\omega} = \nabla \times \boldsymbol{u}$ (cf. [50,51]), Eq. (3.1) in the PPE reformulation can be recast as:

$$\boldsymbol{\omega} = \nabla \times \boldsymbol{u} \qquad \text{in } \Omega, \tag{3.3a}$$

$$\boldsymbol{u}_t = \nu(\nabla(\nabla \cdot \boldsymbol{u}) - \nabla \times \boldsymbol{\omega}) - \nabla P(\boldsymbol{u}) + \boldsymbol{f} \qquad \text{in } \Omega, \tag{3.3b}$$

$$\boldsymbol{n} \times \boldsymbol{u} = \boldsymbol{n} \times \boldsymbol{g} \qquad \text{on } \partial\Omega, \tag{3.3c}$$

$$\nabla \cdot \boldsymbol{u} = 0 \qquad \text{on } \partial\Omega. \tag{3.3d}$$

To obtain the weak formulation of Eqs. (3.3), we use the spaces

$$H(\text{curl}; \Omega) = \left\{ \boldsymbol{u} \in L^2(\Omega)^N : \nabla \times \boldsymbol{u} \in L^2(\Omega)^{N'} \right\},$$
$$H(\text{div}; \Omega) = \left\{ \boldsymbol{u} \in L^2(\Omega)^N : \nabla \cdot \boldsymbol{u} \in L^2(\Omega) \right\},$$

with $N' = 1$ for $N = 2$ and $N' = 3$ for $N = 3$. We then multiply (3.3a) by a test function $\boldsymbol{\tau}$ and (3.3b) by a test function $\boldsymbol{v}$, and then apply the integral identities

$$\langle \nabla \times \boldsymbol{u}, \boldsymbol{\tau} \rangle = \langle \boldsymbol{u}, \nabla \times \boldsymbol{\tau} \rangle + \int_{\partial\Omega} \boldsymbol{\tau} \cdot (\boldsymbol{n} \times \boldsymbol{u}) \, \mathrm{d}S,$$

$$\langle \nabla \times \boldsymbol{\omega} - \nabla(\nabla \cdot \boldsymbol{u}), \boldsymbol{v} \rangle = \langle \nabla \times \boldsymbol{\omega}, \boldsymbol{v} \rangle + \langle \nabla \cdot \boldsymbol{u}, \nabla \cdot \boldsymbol{v} \rangle - \int_{\partial\Omega} (\nabla \cdot \boldsymbol{u})(\boldsymbol{v} \cdot \boldsymbol{n}) \, \mathrm{d}S,$$

along with the tangential boundary condition (3.3c) and the divergence-free boundary condition (3.3d). This procedure yields the following mixed formulation for (3.3): Find $\boldsymbol{\omega} \in X$, $\boldsymbol{u} \in H(\text{div}; \Omega)$ such that

$$\langle \boldsymbol{\omega}, \boldsymbol{\tau} \rangle - \langle \boldsymbol{u}, \nabla \times \boldsymbol{\tau} \rangle = \int_{\partial\Omega} \boldsymbol{\tau} \cdot (\boldsymbol{n} \times \boldsymbol{g}) \, \mathrm{d}S \qquad \forall \boldsymbol{\tau} \in X, \tag{3.4a}$$

$$\langle \boldsymbol{u}_t, \boldsymbol{v} \rangle + \nu \langle \nabla \times \boldsymbol{\omega}, \boldsymbol{v} \rangle + \nu \langle \nabla \cdot \boldsymbol{u}, \nabla \cdot \boldsymbol{v} \rangle = \langle \boldsymbol{f} - \nabla P(\boldsymbol{u}), \boldsymbol{v} \rangle \quad \forall \boldsymbol{v} \in H(\text{div}; \Omega). \tag{3.4b}$$

Here $X = H^1(\Omega)$ when $N = 2$ and $X = H(\text{curl}; \Omega)$ when $N = 3$. Notice that both the tangential boundary condition and the divergence boundary condition from (2.5) appear in the weak form (3.4) as natural boundary conditions (the spaces of functions X and $H(\text{div}; \Omega)$ do not enforce the boundary conditions).

Let Σ^h and V^h be finite dimensional subspaces for X and $H(\text{div}; \Omega)$ respectively. The semi-discrete mixed formulation of (3.4) is as follows: Find $(\boldsymbol{\omega}_h, \boldsymbol{u}_h) \in \Sigma^h \times V^h$ such that $\boldsymbol{u}_h(t = 0) = \boldsymbol{u}_{0h}$ and

$$\langle \boldsymbol{\omega}_h, \boldsymbol{\tau}_h \rangle - \langle \boldsymbol{u}_h, \nabla \times \boldsymbol{\tau}_h \rangle = \int_{\partial\Omega} \boldsymbol{\tau}_h \cdot (\boldsymbol{n} \times \boldsymbol{g}) \, \mathrm{d}S \qquad \forall \boldsymbol{\tau}_h \in \Sigma^h, \tag{3.5a}$$

$$\langle (\boldsymbol{u}_h)_t, \boldsymbol{v}_h \rangle = -\nu \langle \nabla \cdot \boldsymbol{u}_h, \nabla \cdot \boldsymbol{v}_h \rangle - \nu \langle \nabla \times \boldsymbol{\omega}_h, \boldsymbol{v}_h \rangle + \langle \boldsymbol{f} - \nabla P(\boldsymbol{u}_h), \boldsymbol{v}_h \rangle \quad \forall \boldsymbol{v}_h \in V^h, \tag{3.5b}$$

where $\boldsymbol{u}_{0h}$ is the projection of the initial condition $\boldsymbol{u}_0$ onto the space V^h, and $P(\boldsymbol{u}_h)$ is the solution to the discretized pressure Poisson problem using the velocity approximation (see Section 3.2).

There are different stable pairs of finite elements for the spaces Σ^h and V^h [50,52,53]. Here in the case of $N = 2$, we choose nodal finite elements (Lagrange finite elements P_r) of degree $r \geq 1$ for $\boldsymbol{\omega}_h$ and Raviart–Thomas elements (RT_{r-1}) of the same degree for the vector field $\boldsymbol{u}_h$. That is

$$\Sigma^h \times V^h = P_r \times RT_{r-1} \quad \text{for } r \geq 1.$$

In the 3-dimensional case, the corresponding space for $\boldsymbol{\omega}$ is $H(\text{curl}; \Omega)$, and Nédélec elements (NED_r^1) are used.

Remark 3.1 (*Failure of Nodal FEM*)**.** Nodal FEM may fail to converge to the true solution for EBC problems, for two different reasons: (i) the Babuška paradox [54,55], and (ii) the inability to approximate singularities in the solution, such as those caused by re-entrant corners in the domain. The Babuška paradox [54,55] occurs when FEM solutions on polygonal approximations of domains with curved boundaries converge to a function (as the mesh size goes to zero) that is not the solution of the underlying continuum problem. For instance, the vector Laplace problem (with $\nabla \cdot \boldsymbol{f} = 0$)

$$\Delta \boldsymbol{u} = \boldsymbol{f} \quad \text{in } \Omega, \quad \text{with b.c.} \quad \nabla \cdot \boldsymbol{u} = 0 \quad \text{and} \quad \boldsymbol{n} \times \boldsymbol{u} = 0 \quad \text{on } \partial\Omega, \tag{3.6}$$

has the weak formulation: Given $\boldsymbol{f} \in L^2(\Omega)^N$, $\nabla \cdot \boldsymbol{f} = 0$, find $\boldsymbol{u} \in V$, such that for every $\boldsymbol{v} \in V$

$$\langle \nabla \times \boldsymbol{u}, \nabla \times \boldsymbol{v} \rangle + \langle \nabla \cdot \boldsymbol{u}, \nabla \cdot \boldsymbol{v} \rangle = \langle \boldsymbol{f}, \boldsymbol{v} \rangle. \tag{3.7}$$

Nodal FEM approximations based on $V = H^1_{0t}(\Omega)^N = \{\boldsymbol{u} \in H^1(\Omega)^N : \boldsymbol{n} \times \boldsymbol{u}|_{\partial\Omega} = 0\}$ exhibit the Babuška paradox and may not converge to the solution of (3.6) [48].

The second issue with nodal elements is an approximation theory result. The weak formulation (3.7) is uniquely solvable for the following two choices of space: $V = H^1_{0t}(\Omega)^N$ or $V = H_0(\text{curl}; \Omega) \cap H(\text{div}; \Omega) = \{\boldsymbol{u} \in L^2(\Omega)^N : \nabla \cdot \boldsymbol{u} \in L^2(\Omega)^N, \nabla \times \boldsymbol{u} \in L^2(\Omega)^{N'}, \boldsymbol{n} \times \boldsymbol{u}|_{\partial\Omega} = 0\}$. When the domain Ω is convex or has a globally C^2 boundary, then $H^1_{0t}(\Omega)^N = H_0(\text{curl}; \Omega) \cap H(\text{div}; \Omega)$ and the solution is divergence-free. When Ω has re-entrant corners, we have $H^1_{0t}(\Omega)^N \subsetneq H_0(\text{curl}; \Omega) \cap H(\text{div}; \Omega)$ and the divergence-free solution may not in $H^1_{0t}(\Omega)^N$[56]. Hence, in general H^1 nodal FEM is not guaranteed to converge to the divergence-free solution.

3.2. Spatial discretization of the pressure

The pressure p satisfies a Poisson problem with Neumann boundary condition (3.2). Therefore, given the velocity, standard nodal-based finite elements can be used to discretize the pressure Poisson equation. Following the usual procedure for deriving weak formulations, we multiply equation (3.2) by a test function $q \in H^1(\Omega)$ and apply integration by parts to obtain

$$\langle \nabla p, \nabla q \rangle = \langle \boldsymbol{f}, \nabla q \rangle - \nu \int_{\partial\Omega} (\boldsymbol{n} \cdot \nabla \times \nabla \times \boldsymbol{u}) q \, \mathrm{d}S + \lambda \int_{\partial\Omega} \boldsymbol{n} \cdot (\boldsymbol{u} - \boldsymbol{g}) q \, \mathrm{d}S - \int_{\partial\Omega} (\boldsymbol{n} \cdot \boldsymbol{g}_t) q \, \mathrm{d}S.$$

We further substitute $\boldsymbol{\omega} = \nabla \times \boldsymbol{u}$, which gives rise to two possible different weak formulations for the pressure Poisson equation:

1. Choosing the boundary integral that involves $\boldsymbol{n} \cdot (\nabla \times \boldsymbol{\omega})$ yields the first weak formulation

$$\langle \nabla p, \nabla q \rangle = \langle \boldsymbol{f}, \nabla q \rangle - \nu \int_{\partial\Omega} \boldsymbol{n} \cdot (\nabla \times \boldsymbol{\omega}) q \, \mathrm{d}S + \lambda \int_{\partial\Omega} \boldsymbol{n} \cdot (\boldsymbol{u} - \boldsymbol{g}) q \, \mathrm{d}S - \int_{\partial\Omega} (\boldsymbol{n} \cdot \boldsymbol{g}_t) q \, \mathrm{d}S, \quad \forall q \in H^1(\Omega). \tag{3.8}$$

2. Choosing the volume integral of $(\nabla \times \boldsymbol{\omega}) \cdot \nabla q$ gives the second weak formulation

$$\langle \nabla p, \nabla q \rangle = \langle \boldsymbol{f}, \nabla q \rangle - \nu \langle \nabla \times \boldsymbol{\omega}, \nabla q \rangle + \lambda \int_{\partial\Omega} \boldsymbol{n} \cdot (\boldsymbol{u} - \boldsymbol{g}) q \, \mathrm{d}S - \int_{\partial\Omega} (\boldsymbol{n} \cdot \boldsymbol{g}_t) q \, \mathrm{d}S, \quad \forall q \in H^1(\Omega). \tag{3.9}$$

The two formulations (3.8) and (3.9) differ only in one term: (3.9) contains an integral over the domain (i.e. $\langle \nabla \times \boldsymbol{\omega}, \nabla q \rangle$) while (3.8) is the integration by parts of (3.9) which (due to the curl), leaves only an integral along the boundary (i.e. $\int_{\partial\Omega} \boldsymbol{n} \cdot (\nabla \times \boldsymbol{\omega}) q \, \mathrm{d}S$). For spatial discretizations that satisfy a summation-by-parts formula, (3.8) and (3.9) will yield discrete formulations with identical solutions. For spatial discretizations that do not satisfy a summation-by-parts formula, the two terms in (3.8) and (3.9) differ slightly — the difference being due to quadrature errors incurred by the discrete failure to satisfy a summation by parts formula. Algorithmically, solving discretizations of the two formulas lead to some notable differences: the integral over the domain formulation (3.9) involves computing many more quadrature integrals and results in a denser matrix. In numerical tests both choices return almost identical results. Therefore in this paper we show only the results of numerical experiments conducted with the first formulation, (3.8).

3.3. Time discretization via IMEX schemes

One advantage of the PPE reformulation is that the pressure appears as a global function of the velocity in the momentum equation. This enables conceptually straightforward implicit–explicit (IMEX) time discretizations of the PPE system that treat the pressure explicitly and viscosity implicitly. An implicit treatment of the viscosity term is desirable for low to moderate Reynolds numbers as to avoid a parabolic time step stability restriction. In addition, an explicit treatment of the pressure is desirable to avoid solving large coupled systems involving $(p, \boldsymbol{u})$.

IMEX schemes are based on an additive splitting of an ODE that takes the representative form:

$$\frac{\mathrm{d}u}{\mathrm{d}t} = \mathcal{F}(u) + \mathcal{G}(u). \tag{3.10}$$

Popular IMEX methods are linear multistep IMEX schemes [57] and IMEX Runge–Kutta (RK) methods [58]. Here we focus on IMEX RK schemes because they have less restrictive stability properties than IMEX multistep methods. We consider IMEX RK schemes that combine two different Runge–Kutta schemes: an explicit RK (ERK) method for $\mathcal{F}(u)$, and a diagonally implicit RK (DIRK) method for $\mathcal{G}(u)$. Let $A \in \mathbb{R}^{s\times s}$, $\boldsymbol{b}, \boldsymbol{c} \in \mathbb{R}^s$ be the coefficients of an s-stage DIRK scheme, and $\hat{A} \in \mathbb{R}^{(s+1)\times(s+1)}$, $\hat{\boldsymbol{b}}$, $\hat{\boldsymbol{c}} \in \mathbb{R}^{s+1}$ be the coefficients of an $(s+1)$-stage ERK scheme with $\hat{\boldsymbol{c}}^T = (0, \boldsymbol{c}^T)$ in the Butcher notation [59], i.e.

$$\begin{array}{c|c} \boldsymbol{c} & A \\ \hline & \boldsymbol{b}^T \end{array} = \begin{array}{c|ccccc} c_1 & a_{11} & & & & \\ c_2 & a_{21} & a_{22} & & & \\ \vdots & \vdots & \vdots & \ddots & & \\ c_s & a_{s1} & a_{s2} & \cdots & a_{ss} \\ \hline & b_1 & b_2 & \cdots & b_s \end{array} \qquad \begin{array}{c|c} \hat{\boldsymbol{c}} & \hat{A} \\ \hline & \hat{\boldsymbol{b}}^T \end{array} = \begin{array}{c|ccccc} 0 & 0 & & & & \\ c_1 & \hat{a}_{21} & 0 & & & \\ c_2 & \hat{a}_{31} & \hat{a}_{32} & 0 & & \\ \vdots & \vdots & \vdots & \vdots & \ddots & \\ c_s & \hat{a}_{s+1,1} & \hat{a}_{s+1,2} & \hat{a}_{s+1,3} & \cdots & 0 \\ \hline & \hat{b}_1 & \hat{b}_2 & \hat{b}_3 & \cdots & \hat{b}_{s+1} \end{array}$$

One step of an IMEX scheme from time t_n to $t_{n+1} = t_n + \Delta t$ for the splitting (3.10) can be written as follows:

$$u^{(i)} = u^n + \Delta t \sum_{j=1}^{i} a_{ij}\mathcal{G}(u^{(j)}) + \Delta t \sum_{j=1}^{i} \hat{a}_{i+1,j}\mathcal{F}(u^{(j-1)}) \quad \text{for} \quad i = 1, \ldots, s \tag{3.11}$$

$$u^{n+1} = u^n + \Delta t \sum_{i=1}^{s} b_j\mathcal{G}(u^{(j)}) + \Delta t \sum_{j=1}^{s+1} \hat{b}_j\mathcal{F}(u^{(j-1)}) \tag{3.12}$$

where $u^{(0)} = u^n$.

3.3.1. Stability of IMEX Runge–Kutta schemes applied to the time-dependent Stokes equations

IMEX schemes applied to the time-dependent Stokes equations (3.1)–(3.2) (and more generally to the PPE system (2.5)–(2.6)) may encounter subtle stability issues when the pressure is treated explicitly. First we will examine the numerical stability of an IMEX RK scheme applied to a scalar ODE model for the system (3.1)–(3.2). The model problem will then yield a stability criterion, which will dictate our choice of IMEX coefficients.

Using the vector identity $\Delta = \nabla(\nabla\cdot) - \nabla\times\nabla\times$, and introducing $\mathcal{A} := -\nabla\times\nabla\times$, $\mathcal{B} := \nabla(\nabla\cdot)$, the time-dependent Stokes system (3.1)–(3.2) can be (exactly) recast (with $\nu = 1$, when $\boldsymbol{f} = 0$, $\boldsymbol{g} = 0$) as the following non-local evolution

$$\boldsymbol{u}_t = \underbrace{\mathcal{A}\boldsymbol{u} + \mathcal{B}\boldsymbol{u}}_{\mathcal{G}(u)} - \underbrace{\mathcal{P}(\mathcal{A}\boldsymbol{u}) - \lambda\mathcal{P}\boldsymbol{u}}_{\mathcal{F}(u)} \quad \text{in } \Omega \quad \text{with b.c. } \boldsymbol{n}\times\boldsymbol{u} = 0, \quad \nabla\cdot\boldsymbol{u} = 0 \quad \text{on } \partial\Omega. \tag{3.13}$$

Here the operator $\mathcal{P}$ (not to be confused with the pressure operator $P(u)$) is defined by

$$\mathcal{P}\boldsymbol{w} = \nabla p, \tag{3.14}$$

where p solves the Poisson equation

$$\Delta p = 0 \quad \text{in } \Omega, \quad \text{with b.c. } \frac{\partial p}{\partial \boldsymbol{n}} = \boldsymbol{n}\cdot\boldsymbol{w} - \bar{w} \quad \text{on } \partial\Omega, \quad \text{where } \bar{w} := \frac{1}{|\partial\Omega|}\int_{\partial\Omega} \boldsymbol{n}\cdot\boldsymbol{w}\, \mathrm{d}S. \tag{3.15}$$

By definition, $\mathcal{P}\boldsymbol{w}$ generates a divergence-free field, with normal component $\boldsymbol{n}\cdot\boldsymbol{w} - \bar{w}$ at the boundary. It follows that $\mathcal{P}^2 = \mathcal{P}$, i.e. $\mathcal{P}$ is a projection.

We adopt IMEX discretizations of (3.13) that treat $\mathcal{A}\boldsymbol{u} + \mathcal{B}\boldsymbol{u}$ implicitly and $-\mathcal{P}(\mathcal{A}\boldsymbol{u}) - \lambda\mathcal{P}\boldsymbol{u}$ explicitly. Due to the structure of the projection, $\mathcal{P}(\mathcal{A}\boldsymbol{u})$ is stiff since $\mathcal{A}$ has two spatial derivatives (i.e. may incur a parabolic time step restriction). Thus both the implicit term (which includes $\mathcal{A}\boldsymbol{u}$) and the explicit term (∇p, which includes $\mathcal{P}\mathcal{A}\boldsymbol{u}$) are stiff. To investigate the stability of IMEX RK schemes for solving the PPE reformulation, we consider a scalar model problem for Eq. (3.13)

$$u_t = -\gamma u + \mu u, \tag{3.16}$$

where $-\gamma u$ is treated implicitly and μu explicitly. The model equation (3.16) is frequently used to understand IMEX stability. However, commonly one considers $\gamma > 0$ real and μ purely imaginary, e.g. to understand time-stepping

for advection–diffusion problems [57,58]. In contrast, here we interpret γ as an eigenvalue of $-\mathcal{A}\boldsymbol{u}$ and μ as an eigenvalue of $-\mathcal{P}\mathcal{A}\boldsymbol{u}$. Since $-\mathcal{A}$ is symmetric positive semi-definite (in the L^2 inner product on vector fields with EBC), and $\mathcal{P}$ is a projection, the values of γ and μ are both real and non-negative. Moreover, because $\mathcal{P}$ is a projection (and thus has no eigenvalues larger than 1), we consider (3.16) with $0 < \mu \leq \gamma$. The motivation is that if $\mathcal{A}$ and $\mathcal{P}\mathcal{A}$ commute (which they are not guaranteed to do), then they would share the same eigenvectors, i.e. $-\mathcal{A}\boldsymbol{v} = \gamma\boldsymbol{v}$ and $-\mathcal{P}\mathcal{A}\boldsymbol{v} = \mu\boldsymbol{v}$, and hence $\boldsymbol{v}$ would also be an eigenvector of $\mathcal{P}$ with eigenvalue $\mu/\gamma \in \{0, 1\}$. We believe that a more detailed analysis justifying (3.16) that incorporates $\mathcal{B}$, and the fact that the operators involved do not commute, can be done using the methodology introduced in [60], however we will not attempt this here.

The situation $(\gamma, \mu) \in \mathbb{R}^2$ was studied in [61], to understand the stability properties for certain 1st and 2nd order IMEX RK schemes in the context of reaction–diffusion equations. However, both the stiffness behavior and the important wedge property introduced below (see Definition 3.1) were not discussed in [61].

Let us pad the s-stage implicit Runge–Kutta scheme with zeros to obtain the tableau

$$\begin{array}{c|c} \tilde{\boldsymbol{c}} & \tilde{A} \\ \hline & \tilde{\boldsymbol{b}}^T \end{array} = \begin{array}{c|cc} 0 & 0 & 0 \\ \boldsymbol{c} & 0 & A \\ \hline & 0 & \boldsymbol{b}^T \end{array}, \tag{3.17}$$

and introduce the vector $\boldsymbol{U}^{n+1} = (u^n, u_1^{n+1}, \ldots, u_s^{n+1})^T$ that includes the s intermediate stage solutions and the approximation from previous time step. Then one step of the IMEX RK scheme applied to the model problem (3.16) can be expressed as

$$\boldsymbol{U}^{n+1} = u^n\boldsymbol{e} - \gamma\Delta t\tilde{A}\boldsymbol{U}^{n+1} + \mu\Delta t\hat{A}\boldsymbol{U}^{n+1}, \tag{3.18}$$

$$u^{n+1} = u^n - \gamma\Delta t\tilde{\boldsymbol{b}}^T\boldsymbol{U}^{n+1} + \mu\Delta t\hat{\boldsymbol{b}}^T\boldsymbol{U}^{n+1}, \tag{3.19}$$

where $\boldsymbol{e}$ is an $(s+1)$-vector of all ones. The above expressions yield

$$u^{n+1} = R(\gamma\Delta t, \mu\Delta t)u^n, \tag{3.20}$$

where

$$\begin{aligned} R(\alpha, \beta) &= 1 + (-\alpha\tilde{\boldsymbol{b}}^T + \beta\hat{\boldsymbol{b}}^T)(I + \alpha\tilde{A} - \beta\hat{A})^{-1}\boldsymbol{e} \\ &= \frac{\det(I + \alpha\tilde{A} - \beta\hat{A} - \alpha\boldsymbol{e}\tilde{\boldsymbol{b}}^T + \beta\boldsymbol{e}\hat{\boldsymbol{b}}^T)}{\det(I + \alpha\tilde{A} - \beta\hat{A})}. \end{aligned}$$

is the IMEX RK analogue of the stability function for Runge–Kutta schemes applied to the test problem $y' = \lambda y$. It is now natural to define the *stability region* as

$$S = \{(\alpha, \beta) : |R(\alpha, \beta)| \leq 1\}. \tag{3.21}$$

For a given IMEX RK scheme, we can plot the stability region in the (α, β)-plane, where $\alpha = \gamma\Delta t$ and $\beta = \mu\Delta t$. In general, when both γ and μ are in $\mathbb{C}$, the stability region S is a subset in $\mathbb{C}^2$. For the model problem (3.16), it suffices to look at the cross section of the region S in the first quadrant of $\mathbb{R}^2$, which can be easily visualized.

Definition 3.1. An IMEX RK scheme is said to possess the wedge property, if the stability region S contains the wedge $\{(\alpha, \beta) : 0 < \beta \leq \alpha\}$. In other words, the scheme is unconditionally stable for the model problem (3.16) with any $0 < \mu \leq \gamma$.

A third-order IMEX RK method that satisfies the wedge property is the scheme denoted IMEX(4,4,3) in [58]. It possesses 4 implicit stages and 4 explicit stages and has the Butcher tableau

$$\begin{array}{c|c} \boldsymbol{c} & A \\ \hline & \boldsymbol{b}^T \end{array} = \begin{array}{c|cccc} 1/2 & 1/2 & & & \\ 2/3 & 1/6 & 1/2 & & \\ 1/2 & -1/2 & 1/2 & 1/2 & \\ 1 & 3/2 & -3/2 & 1/2 & 1/2 \\ \hline & 3/2 & -3/2 & 1/2 & 1/2 \end{array}, \qquad \begin{array}{c|c} \hat{\boldsymbol{c}} & \hat{A} \\ \hline & \hat{\boldsymbol{b}}^T \end{array} = \begin{array}{c|ccccc} 0 & 0 & & & & \\ 1/2 & 1/2 & 0 & & & \\ 2/3 & 11/18 & 1/18 & 0 & & \\ 1/2 & 5/6 & -5/6 & 1/2 & 0 & \\ 1 & 1/4 & 7/4 & 3/4 & -7/4 & 0 \\ \hline & 1/4 & 7/4 & 3/4 & -7/4 & 0 \end{array}. \tag{3.22}$$

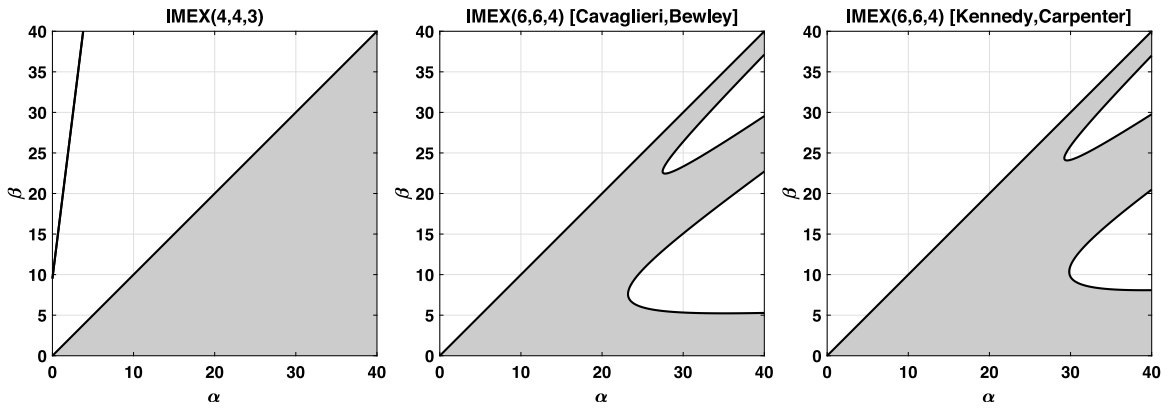

Fig. 1. Stability regions of three IMEX RK schemes for the scalar test problem $u_t = -\gamma u + \mu u$. Left to right: 3rd order IMEX(4,4,3); 4th order IMEX RK scheme by Cavaglieri and Bewley [62]; 4th order IMEX RK scheme by Kennedy and Carpenter [63].

Note that the explicit RK scheme $(\hat{A}, \hat{\boldsymbol{b}}, \hat{\boldsymbol{c}})$ is a 4-stage scheme recast as a 5-stage scheme which is stiffly accurate (the last row of $\hat{A}$ equals the vector $\hat{\boldsymbol{b}}^T$). This scheme is suitable for the PPE reformulation as it is unconditionally stable when solving the linear model problem (3.16) (see the left panel in Fig. 1 for the stability region). We therefore adopt the 3rd order IMEX RK scheme (3.22) for all numerical computations in this paper.

We are unaware of any existing 4th order (or higher) schemes that satisfy the wedge property. For instance, two popular 4th order IMEX RK schemes, one by Cavaglieri and Bewley [62] and the other by Kennedy and Carpenter [63], both violate the wedge property (see Fig. 1 middle and right panels).

Note that the wedge property is a sufficient condition for unconditional stability of the IMEX RK scheme for only the model problem (3.16) with $0 < \mu \leq \gamma$. Nevertheless, this condition can provide insight into the stability property of a given IMEX RK scheme also for the PPE reformulation (2.5)–(2.6). For instance, we generally observe that 4th order schemes violating the wedge property require a stiff parabolic time step restriction $\Delta t = O(\Delta x^2)$.

As a final comment on the RK time discretization, RK schemes (including IMEX RK schemes) suffer from order reduction when applied to initial boundary value problems with time-dependent boundary conditions or forcings on the boundary [64–66]. We summarize the order reduction phenomena in the following remark.

Remark 3.2. Order reduction is a generic problem of RK schemes where the observed temporal convergence rate is lower than the formal order of the scheme. Order reduction is often due to the formation of numerical boundary layers, caused by enforcing boundary conditions in the RK scheme [67]. While several approaches exist to remedy order reduction [63,66–69], they do not easily generalize to PPE reformulations or IMEX settings.

To investigate the high order accuracy of the methods presented in this paper, we choose specific test problems (below) in which the structure of the problem does not lead to order reduction. Because order reduction is a generic phenomenon that is not specific to PPE reformulations, the (important) question of how to avoid order reduction is of generic nature and not specific to this work.

It is worth pointing out that IMEX multistep methods are devoid of order reduction. A key obstacle to the applicability of multistep methods has been their restrictive stability properties, particularly for problems in which the implicit and explicit parts are both stiff [70], such as PPE reformulations. However, recently proposed IMEX multistep methods [60] can achieve unconditional stability for such problems, and thus may provide an alternative suitable time-stepping strategy for PPE reformulations.

3.4. Numerical results for the vector heat equation and time-dependent Stokes equations

Collectively, Sections 3.1–3.3 give rise to the following numerical scheme.

Numerical Scheme 1. *Time-dependent Stokes equation (rth order in space, 3rd order in time).*

1. *Spatial discretization of velocity and pressure via method of lines (MOL) to yield an ODE IVP:*
   - *(Mixed FEM velocity spaces) Discretize* $(\boldsymbol{\omega}_h, \boldsymbol{u}_h) \in \Sigma^h \times V^h$ *where for* $N = 2$, $\Sigma^h \times V^h = P_r \times RT_{r-1}$ *with triangular mesh, and for* $N = 3$, $\Sigma^h \times V^h = NED_r^1 \times RT_{r-1}$ *with tetrahedral mesh to yield the ODE equations (3.5).*
   - *(Initial data) Set* $\boldsymbol{u}_h(t = 0) = \boldsymbol{u}_{0h}$ *as initial date* $\boldsymbol{u}_0$ *projected onto the space* V^h*;*
   - *(FEM pressure spaces) Discretize* $p_h \in P_r$ *in (3.8) using standard nodal FEM.*

   Together, the MOL discretization yields Eqs. (3.5)–(3.8) and defines an IVP.
2. *Time-discretize (3.5)–(3.8) via 3rd order IMEX (4,4,3) (with coefficients in (3.22)). In the IMEX scheme steps (3.11), the implicit and explicit parts are given by:*

$$\mathcal{G}(u^n) \leftarrow -\nu\langle \nabla \cdot \boldsymbol{u}_h, \nabla \cdot \boldsymbol{v}_h\rangle - \nu\langle \nabla \times \boldsymbol{\omega}_h, \boldsymbol{v}_h\rangle,$$
$$\mathcal{F}(u^n) \leftarrow \langle \boldsymbol{f} - \nabla P(\boldsymbol{u}_h), \boldsymbol{v}_h\rangle.$$

3. *Time-advance the full space–time discretized scheme. At each RK stage time-step, the mixed FEM variables* $(\boldsymbol{\omega}_h, \boldsymbol{u}_h)$ *solve a saddle-point system; and the pressure variables* p_h *solve a linear system.*

The goal of this subsection is to demonstrate via numerical examples that, for the time-dependent Stokes problem (3.1)–(3.2), the proposed method can achieve high-order in space and third order in time. We employ the method of manufactured solutions and conduct convergence studies for the spatial accuracy (see Section 3.4.2), the temporal accuracy for the 3rd order IMEX(4,4,3) scheme (3.22) (see Section 3.4.3), and the accuracy of the overall scheme (see Section 3.4.4).

We implement the numerical methods using the software package FEniCS [71], which contains an extensive library of finite elements through one of its components: Finite element Automatic Tabulator (FIAT) [72,73]. It provides $H(\text{div})$ element spaces such as Raviart–Thomas (RT) elements and $H(\text{curl})$ elements of the Nédélec types. The triangular meshes used for the computations are generated by the software package Gmsh [74]. Throughout this section, the linear equations for $(\boldsymbol{\omega}, \boldsymbol{u})$, and Poisson equation for p, are solved using the built-in FEniCS sparse direct solver. In the latter Navier–Stokes test cases (Sections 4.3.1 and 4.3.4), preconditioned GMRES, with a very small error tolerance and incomplete LU preconditioner, is used for the linear solvers.

3.4.1. Numerical results for the vector heat equation with EBC

Before presenting the results for the PPE reformulation, we show the convergence results for the vector heat equation (VHE) with EBC as a benchmark. This provides both: a baseline for the PPE reformulation convergence study, and a verification of the code. Let the problem domain be $\Omega = [0, 1) \times [0, 1]$ with periodic b.c. applied in the x-direction and EBC in the y-direction. Hence, we apply the Numerical Scheme 1 to the VHE (i.e. pressure is set to zero):

$$\boldsymbol{u}_t = \Delta \boldsymbol{u} + \boldsymbol{f} \qquad \text{for } (x, y) \in (0, 1)^2, \tag{3.23a}$$
$$\boldsymbol{n} \times \boldsymbol{u} = 0, \quad \nabla \cdot \boldsymbol{u} = 0 \qquad \text{for } (x, y) \in [0, 1) \times \{0, 1\}, \tag{3.23b}$$
$$\boldsymbol{u}(0, y) = \boldsymbol{u}(1, y) \qquad \text{for } 0 < y < 1. \tag{3.23c}$$

The divergence-free manufactured solution $\boldsymbol{u} = (u, v)^T = (\psi_y, -\psi_x)^T$ is generated by the stream function

$$\psi(x, y, t) = \cos(t)\sin(4\pi(x + y))(4y(1 - y))^4.$$

The manufactured solution is selected so that the velocity field and its derivatives up to certain order vanish at the boundary to suppress the effect of order reduction due to the IMEX RK time-stepping (Remark 3.2).

To conduct a spatial convergence study we use a series of regular meshes with total number of elements 64, 256, 1024, 4096, and 16 384. For the time evolution we use the third order IMEX (4,4,3) scheme with a fixed small time step $\Delta t = 10^{-5}$ (so that the error due to the time-stepping is negligible) and a fixed final time $T = 10^{-3}$ (100 time steps). The FE spaces are chosen to be $(\boldsymbol{\omega}_h, \boldsymbol{u}_h) \in P_r \times RT_{r-1}$, with degrees $r = 1, 2, 3, 4, 5$. The observed spatial

Table 1
Observed spatial convergence rates in the L^2 norm for the vector heat equation with electric boundary conditions (3.23). The spatial approximation orders are $r = 1, 2, 3, 4, 5$.

Spatial approximation order $r = 1$, $(\boldsymbol{\omega}_h, \boldsymbol{u}_h) \in P_1 \times RT_0$								
Δx	$\boldsymbol{u}$	Rate	$\nabla \cdot \boldsymbol{u}$	Rate	$\boldsymbol{\omega}$	Rate	$\nabla \times \boldsymbol{\omega}$	Rate
2.50E−01	6.93E+00	—	9.97E+00	—	1.37E+02	—	2.76E+03	—
1.25E−01	3.26E+00	1.09	5.64E+00	0.82	3.19E+01	2.10	1.45E+03	0.92
6.25E−02	1.65E+00	0.98	1.04E+00	2.43	7.34E+00	2.12	7.24E+02	1.00
3.13E−02	8.24E−01	1.00	1.97E−01	2.41	1.77E+00	2.05	3.62E+02	1.00
1.56E−02	4.12E−01	1.00	4.57E−02	2.10	4.37E−01	2.01	1.81E+02	1.00
7.81E−03	2.06E−01	1.00	1.12E−02	2.03	1.09E−01	2.00	9.05E+01	1.00
Spatial approximation order $r = 2$, $(\boldsymbol{\omega}_h, \boldsymbol{u}_h) \in P_2 \times RT_1$								
Δx	$\boldsymbol{u}$	Rate	$\nabla \cdot \boldsymbol{u}$	Rate	$\boldsymbol{\omega}$	Rate	$\nabla \times \boldsymbol{\omega}$	Rate
2.50E−01	2.13E+00	—	8.82E+00	—	2.46E+01	—	1.25E+03	—
1.25E−01	7.89E−01	1.43	1.27E+00	2.80	7.50E+00	1.71	3.97E+02	1.66
6.25E−02	2.13E−01	1.89	2.31E−01	2.46	1.99E+00	1.91	1.04E+02	1.94
3.13E−02	5.45E−02	1.97	3.09E−02	2.90	5.01E−01	1.99	2.62E+01	1.98
1.56E−02	1.37E−02	1.99	3.92E−03	2.98	1.25E−01	2.00	6.57E+00	2.00
Spatial approximation order $r = 3$, $(\boldsymbol{\omega}_h, \boldsymbol{u}_h) \in P_3 \times RT_2$								
Δx	$\boldsymbol{u}$	Rate	$\nabla \cdot \boldsymbol{u}$	Rate	$\boldsymbol{\omega}$	Rate	$\nabla \times \boldsymbol{\omega}$	Rate
2.50E−01	1.32E+00	—	3.58E+00	—	1.88E+01	—	6.28E+02	—
1.25E−01	1.28E−01	3.37	2.27E−01	3.98	1.26E+00	3.90	7.40E+01	3.09
6.25E−02	1.56E−02	3.04	1.55E−02	3.87	7.96E−02	3.99	8.46E+00	3.13
3.13E−02	1.92E−03	3.02	9.67E−04	4.00	5.05E−03	3.98	1.05E+00	3.02
1.56E−02	2.40E−04	3.00	6.03E−05	4.00	3.17E−04	3.99	1.30E−01	3.00
Spatial approximation order $r = 4$, $(\boldsymbol{\omega}_h, \boldsymbol{u}_h) \in P_4 \times RT_3$								
Δx	$\boldsymbol{u}$	Rate	$\nabla \cdot \boldsymbol{u}$	Rate	$\boldsymbol{\omega}$	Rate	$\nabla \times \boldsymbol{\omega}$	Rate
2.50E−01	2.41E−01	—	1.68E+00	—	2.64E+00	—	1.52E+02	—
1.25E−01	1.74E−02	3.80	6.54E−02	4.68	1.70E−01	3.96	1.01E+01	3.91
6.25E−02	1.20E−03	3.85	1.04E−03	5.97	1.35E−02	3.66	6.98E−01	3.86
3.13E−02	7.73E−05	3.96	4.34E−05	4.58	8.98E−04	3.91	4.50E−02	3.95
1.56E−02	4.87E−06	3.99	2.27E−06	4.26	5.70E−05	3.98	2.84E−03	3.99
Spatial approximation order $r = 5$, $(\boldsymbol{\omega}_h, \boldsymbol{u}_h) \in P_5 \times RT_4$								
Δx	$\boldsymbol{u}$	Rate	$\nabla \cdot \boldsymbol{u}$	Rate	$\boldsymbol{\omega}$	Rate	$\nabla \times \boldsymbol{\omega}$	Rate
2.50E−01	8.56E−02	—	4.14E−01	—	1.27E+00	—	4.39E+01	—
1.25E−01	2.16E−03	5.31	7.33E−03	5.82	2.86E−02	5.48	1.47E+00	4.90
6.25E−02	6.31E−05	5.10	5.62E−05	7.03	4.64E−04	5.94	4.13E−02	5.15
3.13E−02	1.92E−06	5.04	8.70E−07	6.01	7.52E−06	5.95	1.27E−03	5.03
1.56E−02	5.97E−08	5.01	1.36E−08	6.00	1.19E−07	5.99	3.93E−05	5.01

rates of convergence in the L^2 norm are shown in Table 1 (the same rates are observed in the L^∞ norm). These results confirm the error estimate for the semi-discrete (in space) VHE in [51] where the quantities $\boldsymbol{u}$, $\nabla \cdot \boldsymbol{u}$, $\boldsymbol{\omega}$ and $\nabla \times \boldsymbol{\omega}$ were proved to be at least rth order convergent for rth order finite elements.

The observed convergence rates are clean, with the exception of $r = 4$ which shows some degradation in the convergence of $\nabla \cdot \boldsymbol{u}$. Even though they do not contradict the existing error estimates, there are some convergence patterns that are worth commenting on:

1. The spatial convergence result for $\boldsymbol{\omega}$ exhibits an even–odd behavior. Specifically, the rate is r for even order r, and it is $r + 1$ when r is odd.
2. Extra orders of convergence (in space) for $\nabla \cdot \boldsymbol{u}$ are observed for both the VPE and the VHE problems when the exact solution satisfies $\nabla \cdot \boldsymbol{u} = 0$. When the exact solutions are not divergence-free, there are no extra convergence orders for the divergence; however, $\nabla \cdot \boldsymbol{u} = 0$ is the common situation for incompressible fluid flows, so the extra order is noteworthy.

Now that we have established the convergence results for the VHE with EBC, and compared them with the existing error estimates, we move on to the PPE reformulation. Note that, in this case, theoretical convergence results are not available. We numerically investigate the performance of the proposed schemes.

3.4.2. Spatial accuracy of the time-dependent Stokes problem

We now conduct a spatial convergence study of the proposed method for the time-dependent Stokes PPE (3.1)–(3.2) discretized in space according to (3.5) and (3.8) and in time via the IMEX RK scheme (3.22). We consider the same domain, $\Omega = [0, 1) \times [0, 1]$, with periodic b.c. in the x-direction, EBC in the y-direction, and the same divergence-free velocity profile, $\boldsymbol{u}(x, y, t)$, as in Section 3.4.1. The pressure is taken to be

$$p = \cos(t)\cos(4\pi(x + y))(4y(1 - y))^4.$$

The forcing is fixed as $\boldsymbol{f} = \boldsymbol{u}_t - \nu\Delta\boldsymbol{u} + \nabla p$, and the initial conditions are chosen as $\boldsymbol{u}_0 = \boldsymbol{u}(x, y, 0)$ (to match the manufactured solution). Both the manufactured solution and the forcing vanish at the boundary.

Following the same procedure as with the VHE above, we select the FE space $(\boldsymbol{\omega}_h, \boldsymbol{u}_h, p_h) \in P_r \times RT_{r-1} \times P_r$, with degrees $r = 1, 2, 3, 4, 5$ on regular meshes. The time-stepping is done via IMEX(4,4,3), with fixed time step $\Delta t = 10^{-5}$ and final time $T = 10^{-3}$. The stabilization parameter λ is set to be 10, in line with the suggestion in [42] and discussed in detail in Section 3.4.5.

For the finest mesh resolution, and the 5th order spatial approximation, the sizes of the matrices for $(\boldsymbol{\omega}, \boldsymbol{u})$ and p are $656\,000 \times 656\,000$ and $205\,121 \times 205\,121$, respectively, which is close to the maximum that the direct solver can handle reliably.

Table 2 shows the spatial error convergence results for different degrees of the spatial approximation. The approximation errors are measured in the L^2 norm. For quantities related to $\boldsymbol{u}$ and $\boldsymbol{\omega}$, the rates of convergence have similar behaviors as for the VHE. Specifically: (i) the velocity $\boldsymbol{u}$ is rth order convergent for an rth order spatial approximation, and (ii) the extra convergence orders for $\nabla \cdot \boldsymbol{u}$ is carried over to the PPE reformulation. The convergence rate for the pressure p behaves similarly to $\boldsymbol{\omega}$, which appears in the right hand side of the weak formulation for the pressure in (3.8) and (3.9). However, non-clean pressure convergence rates are observed for approximation orders larger then 2.

It should be stressed that we numerically measure the convergence rate for the error in the velocity gradient $\nabla\boldsymbol{u}$, even though the FEM spaces do not guarantee that $\nabla\boldsymbol{u}_h$ is in L^2. In particular, the numerical solution for the velocity is, generally, discontinuous (in the tangential direction) across Raviart–Thomas element edges. Here we measure the error in $\nabla\boldsymbol{u}_h$ by ignoring the jumps across the edges, i.e. by only counting the error within each element. Note that it is of interest to measure the accuracy of velocity gradients as they relate to fluid stresses and forces at the boundary of objects. In addition, measuring the accuracy of fluid gradients will be a precursor to Section 4, in which $\boldsymbol{u} \cdot \nabla\boldsymbol{u}$ will be included in the equations.

3.4.3. Temporal accuracy of the time-dependent Stokes problem

To check the temporal accuracy, we consider a manufactured solution on the same domain $\Omega = [0, 1) \times [0, 1]$ with periodicity in the x-direction. The manufactured solution follows from the stream function

$$\psi(x, y, t) = \cos(200t)\sin^2(\pi x)\sin^2(\pi y),$$

so that the divergence-free condition is automatically satisfied by the velocity field $\boldsymbol{u} = (u, v)^T = (\psi_y, -\psi_x)^T$. The pressure is

$$p(x, y, t) = \cos(200t)\sin(2\pi x)\sin(\pi y).$$

Again, note that both the solution and the forcing vanish at the domain boundary. To test the temporal errors, we select a highly oscillatory in time manufactured solution. The high frequency oscillations in time ensure that the time discretization errors dominate the spatial discretization errors for the mesh resolution we use.

To perform the temporal error convergence study we solve the linear problem on a fixed mesh (mesh size $\Delta x = 3.125 \times 10^{-2}$ and 4096 elements), a fixed FE discretization scheme (FE space with degree 4, that is $(\boldsymbol{\omega}_h, \boldsymbol{u}_h, p_h) \in P_4 \times RT_3 \times P_4$), and a final time $T = 0.5$. Then we vary the time step: $\Delta t = 2^{-k}$, $k = 7, \ldots, 13$.

The temporal convergence results for the 3rd order IMEX(4,4,3) scheme are shown in Table 3. All quantities, except for the divergence $\nabla\cdot\boldsymbol{u}$, exhibit a 3rd order convergence in time in the L^2 norm, while $\nabla\cdot\boldsymbol{u}$ remains small for all Δt. The stagnation in the convergence for $\nabla\boldsymbol{u}$, at $O(10^{-4})$, is due to the spatial approximation error dominating the temporal error.

Table 2
Spatial error convergence in the L^2 norm for the time-dependent Stokes equations (3.1)–(3.2) in Section 3.4.2. The spatial approximations are $(\boldsymbol{\omega}_h, \boldsymbol{u}_h, p_h) \in P_r \times RT_{r-1} \times P_r$, with degrees $r = 1, 2, 3, 4, 5$. The calculations are done using $\lambda = 10$ and the 3rd order IMEX(4,4,3), with a fixed small time step $\Delta t = 10^{-5}$ and a fixed final time $T = 10^{-3}$.

Spatial approximation order $r = 1$, $(\boldsymbol{\omega}_h, \boldsymbol{u}_h, p_h) \in P_1 \times RT_0 \times P_1$										
Δx	$\boldsymbol{u}$	Rate	$\nabla \cdot \boldsymbol{u}$	Rate	$\nabla \boldsymbol{u}$	Rate	$\boldsymbol{\omega}$	Rate	p	Rate
2.50E−01	6.93E+00	—-	1.45E+01	—-	1.37E+02	—-	1.37E+02	—-	3.39E+01	—-
1.25E−01	3.26E+00	1.09	6.13E+00	1.25	1.37E+02	0.00	3.19E+01	2.10	3.38E+00	3.33
6.25E−02	1.65E+00	0.98	1.05E+00	2.54	1.37E+02	0.00	7.33E+00	2.12	4.41E−01	2.94
3.13E−02	8.24E−01	1.00	1.96E−01	2.42	1.37E+02	0.00	1.77E+00	2.05	1.08E−01	2.03
1.56E−02	4.12E−01	1.00	4.57E−02	2.10	1.37E+02	0.00	4.37E−01	2.01	2.71E−02	1.99
7.81E−03	2.06E−01	1.00	1.12E−02	2.02	1.37E+02	0.00	1.09E−01	2.00	6.78E−03	2.00
Spatial approximation order $r = 2$, $(\boldsymbol{\omega}_h, \boldsymbol{u}_h, p_h) \in P_2 \times RT_1 \times P_2$										
Δx	$\boldsymbol{u}$	Rate	$\nabla \cdot \boldsymbol{u}$	Rate	$\nabla \boldsymbol{u}$	Rate	$\boldsymbol{\omega}$	Rate	p	Rate
2.50E−01	2.09E+00	—-	7.40E+00	—-	9.33E+01	—-	2.46E+01	—-	1.80E+01	—-
1.25E−01	7.88E−01	1.41	1.30E+00	2.51	6.25E+01	0.58	7.50E+00	1.71	7.64E−01	4.56
6.25E−02	2.13E−01	1.89	2.41E−01	2.43	3.27E+01	0.93	1.99E+00	1.91	6.18E−02	3.63
3.13E−02	5.45E−02	1.97	3.12E−02	2.95	1.66E+01	0.98	5.01E−01	1.99	1.05E−02	2.56
1.56E−02	1.37E−02	1.99	3.93E−03	2.99	8.33E+00	0.99	1.25E−01	2.00	2.45E−03	2.09
7.81E−03	3.43E−03	2.00	4.92E−04	3.00	4.17E+00	1.00	3.13E−02	2.00	6.08E−04	2.01
Spatial approximation order $r = 3$, $(\boldsymbol{\omega}_h, \boldsymbol{u}_h, p_h) \in P_3 \times RT_2 \times P_3$										
Δx	$\boldsymbol{u}$	Rate	$\nabla \cdot \boldsymbol{u}$	Rate	$\nabla \boldsymbol{u}$	Rate	$\boldsymbol{\omega}$	Rate	p	Rate
2.50E−01	1.33E+00	—-	3.81E+00	—-	7.09E+01	—-	1.88E+01	—-	4.33E+00	—-
1.25E−01	1.28E−01	3.38	2.27E−01	4.07	1.67E+01	2.09	1.26E+00	3.90	1.46E−01	4.89
6.25E−02	1.56E−02	3.04	1.51E−02	3.92	4.24E+00	1.98	7.97E−02	3.99	6.91E−03	4.40
3.13E−02	1.92E−03	3.02	9.58E−04	3.97	1.06E+00	2.00	5.05E−03	3.98	2.96E−04	4.54
1.56E−02	2.40E−04	3.00	6.01E−05	4.00	2.66E−01	2.00	3.17E−04	4.00	1.47E−05	4.34
7.81E−03	2.99E−05	3.00	3.76E−06	4.00	6.65E−02	2.00	1.98E−05	4.00	9.81E−07	3.90
Spatial approximation order $r = 4$, $(\boldsymbol{\omega}_h, \boldsymbol{u}_h, p_h) \in P_4 \times RT_3 \times P_3$										
Δx	$\boldsymbol{u}$	Rate	$\nabla \cdot \boldsymbol{u}$	Rate	$\nabla \boldsymbol{u}$	Rate	$\boldsymbol{\omega}$	Rate	p	Rate
2.50E−01	2.41E−01	—-	1.66E+00	—-	1.94E+01	—-	2.66E+00	—-	1.17E+00	—-
1.25E−01	1.74E−02	3.79	6.23E−02	4.74	3.03E+00	2.68	1.75E−01	3.92	4.83E−02	4.60
6.25E−02	1.20E−03	3.86	1.01E−03	5.95	4.04E−01	2.91	1.38E−02	3.67	3.00E−03	4.01
3.13E−02	7.73E−05	3.96	4.31E−05	4.55	5.14E−02	2.97	9.03E−04	3.93	1.12E−04	4.74
1.56E−02	4.87E−06	3.99	2.26E−06	4.25	6.46E−03	2.99	5.71E−05	3.98	4.62E−06	4.60
Spatial approximation order $r = 5$, $(\boldsymbol{\omega}_h, \boldsymbol{u}_h, p_h) \in P_5 \times RT_4 \times P_5$										
Δx	$\boldsymbol{u}$	Rate	$\nabla \cdot \boldsymbol{u}$	Rate	$\nabla \boldsymbol{u}$	Rate	$\boldsymbol{\omega}$	Rate	p	Rate
2.50E−01	8.61E−02	—	4.24E−01	—	6.56E+00	—	1.31E+00	—	4.88E−01	—
1.25E−01	2.17E−03	5.31	7.49E−03	5.82	4.80E−01	3.77	3.10E−02	5.40	1.36E−02	5.16
6.25E−02	6.33E−05	5.10	5.48E−05	7.10	3.14E−02	3.94	7.41E−04	5.39	5.86E−04	4.54
3.13E−02	1.93E−06	5.04	8.73E−07	5.97	1.98E−03	3.99	2.31E−05	5.00	2.19E−05	4.74
1.56E−02	5.97E−08	5.01	1.53E−08	5.83	1.24E−04	4.00	6.81E−07	5.09	6.70E−07	5.03

Table 3
Temporal error convergence for (3.1)–(3.2) in the L^2 norm for the 3rd order IMEX(4,4,3), on a fixed mesh, with the 4th order spatial discretization $P_4 \times RT_3 \times P_4$. The convergence rates in parentheses stagnate due to the spatial error dominating the temporal error.

Δt	$\boldsymbol{u}$	Rate	$\nabla \cdot \boldsymbol{u}$	Rate	$\nabla \boldsymbol{u}$	Rate	$\boldsymbol{\omega}$	Rate	p	Rate
7.81E−03	7.725935E−02	—	6.531237E−08	—	5.932904E−01	—	5.932850E−01	—	9.039549E−02	—
3.91E−03	9.910506E−03	2.96	3.476197E−08	(0.91)	7.625508E−02	2.96	7.624960E−02	2.96	2.074725E−02	2.12
1.95E−03	1.269255E−03	2.97	3.004490E−08	(0.21)	9.693504E−03	2.98	9.685865E−03	2.98	3.396972E−03	2.61
9.77E−04	1.616344E−04	2.97	3.032122E−08	(−0.01)	1.233570E−03	2.97	1.207865E−03	3.00	4.883108E−04	2.80
4.88E−04	2.073504E−05	2.96	3.101061E−08	(−0.03)	2.734583E−04	(2.17)	1.495803E−04	3.01	6.545107E−05	2.90
2.44E−04	2.760336E−06	2.91	3.146726E−08	(−0.02)	2.270653E−04	(0.27)	1.894479E−05	2.98	8.380049E−06	2.97
1.22E−04	4.870641E−07	(2.50)	3.171521E−08	(−0.01)	2.259969E−04	(0.01)	2.585832E−06	(2.87)	1.032259E−06	3.02

Table 4
Error convergence for the linear problem without the advection term (3.1)–(3.2) in the L^2 norm (top) and the L^∞ norm (bottom). The problem is solved with the 3rd order IMEX RK scheme (IMEX(4,4,3)), the 3rd order spatial discretization $P_3 \times RT_2 \times P_3$, and $\lambda = 30$.

Error convergence in the L^2 norm

Δx	$\boldsymbol{u}$	Rate	$\nabla \cdot \boldsymbol{u}$	Rate	$\nabla \boldsymbol{u}$	Rate	$\boldsymbol{\omega}$	Rate	$\nabla \times \boldsymbol{\omega}$	Rate	p	Rate	∇p	Rate
2.50E−01	4.27E−02	—	9.84E−02	—	2.91E+00	—	3.22E−01	—	1.40E+01	—	1.99E−01	—	5.37E+00	—
1.25E−01	8.12E−03	2.39	8.25E−03	3.57	1.03E+00	1.51	2.48E−02	3.70	2.08E+00	2.75	2.76E−03	6.17	2.11E−01	4.67
6.25E−02	1.04E−03	2.96	5.87E−04	3.81	2.62E−01	1.97	2.81E−03	3.14	2.76E−01	2.91	3.53E−04	2.96	3.09E−02	2.77
3.13E−02	1.33E−04	2.97	3.76E−05	3.96	6.57E−02	2.00	4.57E−04	2.62	3.56E−02	2.96	9.88E−05	1.84	5.14E−03	2.59
1.56E−02	1.69E−05	2.97	2.37E−06	3.99	1.64E−02	2.00	7.66E−05	2.58	4.56E−03	2.96	2.33E−05	2.08	6.73E−04	2.93
7.81E−03	2.14E−06	2.99	1.49E−07	3.99	4.11E−03	2.00	1.14E−05	2.74	5.83E−04	2.97	2.91E−06	3.00	7.65E−05	3.13

Error convergence in the L^∞ norm

Δx	$\boldsymbol{u}$	Rate	$\nabla \cdot \boldsymbol{u}$	Rate	$\nabla \boldsymbol{u}$	Rate	$\boldsymbol{\omega}$	Rate	$\nabla \times \boldsymbol{\omega}$	Rate	p	Rate	∇p	Rate
2.50E−01	2.42E−01	—	3.10E−01	—	1.30E+01	—	2.32E+00	—	1.05E+02	—	1.23E+00	—	2.87E+01	—
1.25E−01	1.12E−01	1.12	4.46E−02	2.80	7.80E+00	0.74	1.54E−01	3.91	2.26E+01	2.21	3.44E−02	5.16	1.45E+00	4.31
6.25E−02	1.77E−02	2.65	3.17E−03	3.81	2.12E+00	1.88	1.92E−02	3.01	2.52E+00	3.16	3.99E−03	3.11	4.28E−01	1.76
3.13E−02	2.34E−03	2.92	2.06E−04	3.95	5.36E−01	1.98	2.68E−03	2.84	3.66E−01	2.79	7.06E−04	2.50	9.46E−02	2.18
1.56E−02	2.97E−04	2.98	1.29E−05	4.00	1.34E−01	2.00	4.05E−04	2.73	5.34E−02	2.78	1.26E−04	2.48	1.42E−02	2.74
7.81E−03	3.73E−05	2.99	8.00E−07	4.01	3.35E−02	2.00	6.02E−05	2.75	5.91E−03	3.18	1.52E−05	3.05	2.29E−03	2.63

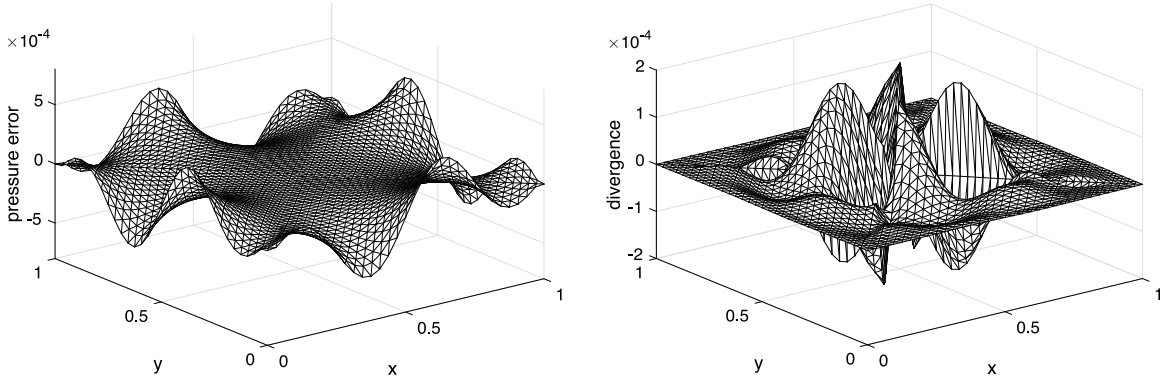

Fig. 2. Errors in the pressure (left) and the divergence (right) for the time-dependent Stokes equations in Section 3.4.4, as functions of (x, y), at the final time $T = 3$. The plot is for the 3rd order IMEX(4,4,3) with a 3rd order ($r = 3$) spatial discretization on a regular mesh with 4096 elements.

3.4.4. Convergence results in both space and time for the time-dependent Stokes equations

Here we present the convergence results for a 3rd order scheme in both space and time applied to the time-dependent Stokes problem (3.1)–(3.2). We use the 3rd order spatial discretization $(\boldsymbol{\omega}_h, \boldsymbol{u}_h, p_h) \in P_3 \times RT_2 \times P_3$ and the 3rd order time-stepping IMEX(4,4,3), with the time step scaled proportional to the mesh size — specifically $\Delta t = 0.2\Delta x$. A series of regular meshes with total number of elements 64, 256, 1024, 4096, 16 384 and 65 536 are used. On the finest mesh, the sizes of the linear systems are 983 808 for $(\boldsymbol{\omega}, \boldsymbol{u})$ and 295 297 for p. The manufactured solution is chosen to be

$$u = \psi_y, \quad v = -\psi_x, \quad p = \pi \cos(t) \cos(\pi x) \sin(\pi y)(4x(1-x))^4(4y(1-y))^4,$$

where $\psi(x, y, t) = \cos(t) \sin^2(\pi x) \sin^2(\pi y)(4x(1-x))^4(4y(1-y))^4$, on the unit square domain $\Omega = [0, 1]^2$. The EBC are prescribed at all boundaries. *This test differs from the previous tests where periodic b.c. in x were used.* Again, the exact solution is constructed so that the velocity and the forcing vanish at the boundary.

Table 4 shows the error convergence results in the L^2 norm (top) and in the L^∞ norm (bottom). Clean convergence is observed for $\boldsymbol{u}$, $\nabla \boldsymbol{u}$ and $\nabla \cdot \boldsymbol{u}$, with rates 3, 2 and 4 respectively. Non-clean convergence rates occur for $\boldsymbol{\omega}$, $\nabla \times \boldsymbol{\omega}$, p and ∇p. However, they appear to be close to 3.

Fig. 2 shows the pressure error and the divergence, as functions of (x, y), at the final time $T = 3$. No numerical boundary layers are observed in the pressure error. The divergence at the final time is small at the boundary, but not exactly zero. This is due to the fact that the divergence boundary condition is only enforced weakly in the mixed formulation (appears as a natural boundary condition). The dynamics of the PPE reformulation ($\nabla \cdot \boldsymbol{u}$ satisfies a heat equation) keeps the divergence small across the domain.

In the PPE reformulation, there is no inf–sup condition for the velocity and the pressure. This is in contrast to the conventional FEM formulation for the Navier–Stokes equations, in which the finite element spaces for the velocity

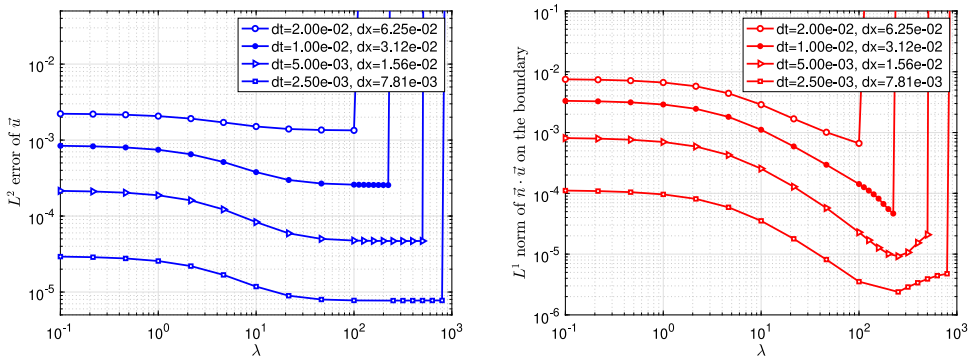

Fig. 3. Velocity error versus λ for different values of Δt and Δx. Left: Velocity error in $L^2(\Omega)$ over the full domain. Right: Velocity flux $\boldsymbol{n}\cdot\boldsymbol{u}$ error along the boundary $L^1(\partial\Omega)$.

and the pressure need to satisfy the discrete version of the inf–sup condition to ensure stability. Hence the orders of the spatial approximations for $(\boldsymbol{\omega}_h, \boldsymbol{u}_h) \in P_r \times RT_{r-1}$ and the pressure $p_h \in P_r$ could be selected independently. However, we observed in the numerical experiments that: *if the pressure approximation is one order less than the velocity approximation, the error convergence for the divergence decreases by one compared to the equal-order case.* Furthermore: *increasing the order of approximation for the pressure does not improve the convergence rates compared to the equal-order case*.

Remark 3.3 (*Degradation of Convergence Rates*)**.** Some of the convergence rates in Table 4 do not exhibit a clear integer rate. A possible explanation for the reduction in convergence rate is provided in [50] (Theorems 5.1–5.2), where it is shown that a mixed finite element approximation for the Stokes equations exhibits a degraded convergence rate.

3.4.5. The choice of parameter λ and its impact on numerical error

Here we present general guidelines on how to choose the parameter λ, based on numerical results and heuristics on how the λ affects the numerical error (along the domain boundary and throughout the domain). The value of λ controls the normal boundary velocity $\boldsymbol{n}\cdot\boldsymbol{u}$. As long as $\lambda > 0$, the solution $\boldsymbol{n}\cdot\boldsymbol{u} = \boldsymbol{n}\cdot\boldsymbol{g}$ to Eq. (2.8) is *asymptotically stable*, i.e. small perturbations in $\boldsymbol{n}\cdot\boldsymbol{u}$ decay back to the correct value $\boldsymbol{n}\cdot\boldsymbol{g}$. When $\lambda = 0$, the ODE for $\boldsymbol{n}\cdot\boldsymbol{u}$ still has the solution $\boldsymbol{n}\cdot\boldsymbol{u} = \boldsymbol{n}\cdot\boldsymbol{g}$, but it is no longer asymptotically stable. Moreover, for the steady state system, the condition $\lambda > 0$ is required to have a unique solution.

We first quantify the effect of λ on the numerical error via a systematic numerical study using the same scheme (3rd order IMEX(4,4,3)) and manufactured solution in Section 3.4.4. Fig. 3 displays the global truncation error (left) and normal boundary flux error (right) versus λ for different choices of $\Delta t \propto \Delta x$.

The key observations are: (i) Both errors decay smoothly with increasing λ until (close to) a stability threshold $\lambda = O(\Delta t^{-1})$, where they increase steeply. (ii) For small λ the boundary error dominates the global error. Then, as λ increases, the global error decreases until saturation, i.e., λ has no further influence anymore on the global error. While the exact λ-value of this desirable saturation regime (which in the figure occurs at $\lambda = O(1)$) depends on the exact nature of the local truncation error constant, in many problems it is observed that λ between 10 and 100 (in non-dimensional units) is a good choice. (iii) For any fixed $\lambda > 0$, the error converges (as $\Delta t \to 0$) at the expected rate for Δt sufficiently small.

These results lead to two natural strategies for choosing λ. The first approach is to choose λ a fixed parameter, independent of the mesh (Δx, Δt) and hitting the saturation region. This way one has a fixed continuum problem and a convergent sequence of numerical approximations (see (iii) above). In all numerical tests conducted here, this simple strategy is employed, with λ between 10 and 100.

An alternative strategy is to minimize the total boundary error by selecting $\lambda = O(\Delta t^{-1})$, with a constant chosen so that one remains safely away from the stability boundary (the steep increase in Fig. 3). This second approach is justified because both errors (at the boundary and the global error) tend to decrease with increasing λ (except for

very close to the stability boundary). It will likely yield smaller boundary flux errors at the expense of now having a sequence of continuum problems with different λ-values.

Next, we provide a theoretical foundation for the behavior seen in Fig. 3 by providing an error bound for an Euler IMEX semi-discretization of the PPE system (accompanied by EBC):

$$\frac{\boldsymbol{u}^{n+1}-\boldsymbol{u}^n}{\Delta t}+\boldsymbol{u}^n\cdot\nabla\boldsymbol{u}^n=\nu\Delta\boldsymbol{u}^{n+1}-\nabla P(\boldsymbol{u}^n)+\boldsymbol{f}^n, \tag{3.24}$$

where $t_n=n\Delta t$, $\boldsymbol{u}^n=\boldsymbol{u}(t_n)$. Note that even in this semi-discrete setting, the divergence $\phi^n=0$ is identically zero for all n (taking the divergence of (3.24) shows that $(I-\nu\Delta t\Delta)\phi^{n+1}=\phi^n$, where $\phi^n=0$ satisfies homogeneous boundary conditions and zero initial data $\phi^0=0$; hence $\phi^n=0$ for all n).

For a fixed $\boldsymbol{x}\in\partial\Omega$, let $g^n=\boldsymbol{n}\cdot\boldsymbol{g}(t_n)$, $g_t^n=\boldsymbol{n}\cdot\boldsymbol{g}_t(t_n)$, $u^n=\boldsymbol{n}\cdot\boldsymbol{u}^n$ and evaluate (3.24) on the boundary (after simplification):

$$\frac{u^{n+1}-u^n}{\Delta t}=-\lambda(u^n-g^n)+g_t^n+\nu\boldsymbol{n}\cdot\Delta(\boldsymbol{u}^{n+1}-\boldsymbol{u}^n). \tag{3.25}$$

Introducing the error $e^n=u^n-g^n$, (3.25) becomes

$$e^{n+1}=Re^n+\Delta t\,\delta^n,\quad \text{where}\quad R=(1-\lambda\Delta t),\ \text{and}\ \delta^n=\nu\Delta(\boldsymbol{u}^{n+1}-\boldsymbol{u}^n)+\underbrace{\Big(g_t^n-\frac{g^{n+1}-g^n}{\Delta t}\Big)}_{\text{LTE}}. \tag{3.26}$$

The values of δ^n consist of two contributions: a local truncation error (LTE) which is $O(\Delta t)$, and a contribution $\Delta(\boldsymbol{u}^{n+1}-\boldsymbol{u}^n)$ that should be of the order of the scheme, $O(\Delta t)$. Hence, if the numerical scheme is such that it satisfies $|\delta^n|\le\Delta t M$ for a constant M, then summing the geometric series defined by (3.26) yields the error estimate:

$$|e^n|\le M\Delta t^2\frac{(1-|R|^n)}{1-|R|}\le\frac{M\,\Delta t}{\lambda},\quad \text{when } e^0=0,\ \text{and } R>0,\ \text{or } \Delta t<\lambda^{-1}. \tag{3.27}$$

Formula (3.27) bounds the error on the boundary as λ^{-1}, a fact that is captured very well in the small Δt curves (for $10\le\lambda\le100$) in the right panel in Fig. 3.

4. Treatment of the nonlinear advection term and Navier–Stokes PPE

Next, in Section 4.1, we explore avenues for discretizing the nonlinear advection term in the mixed finite element framework introduced in Section 3. The numerical results in Section 4.2.1 indicate that the full scheme is convergent, with a little degradation in the rates of convergence relative to the linearized equations. Benchmark test results for the lid-driven cavity and the backward-facing step flow are presented in Section 4.3, which show good agreement with the reference data.

4.1. Discretization of the nonlinear advection term

In Section 3, we introduced a mixed finite element spatial discretization as a way to handle the electric boundary conditions (EBC) for the vector heat equation and time-dependent Stokes equation. While the mixed finite elements resolve several difficulties for the EBC, they come with a caveat: RT elements approximating $\boldsymbol{u}$ are only guaranteed to be continuous across interior edges in the normal direction but can jump in the tangential direction. Therefore, representations of the discrete solution using RT elements are only weakly differentiable along the normal direction across edges. This creates a problem then for handling nonlinear advection terms $\boldsymbol{N}(\boldsymbol{u})=(\boldsymbol{u}\cdot\nabla)\boldsymbol{u}$, and in fact, even linear advection terms $(\boldsymbol{a}\cdot\nabla)\boldsymbol{u}$. Specifically, in 2D, RT elements approximate a function $\boldsymbol{u}$ $\boldsymbol{v}=(v_1,v_2)^T\in H(\mathrm{div};\Omega)$, i.e. $v_1, v_2, \nabla\cdot\boldsymbol{v}\in L^2(\Omega)$. In general, each component of $\nabla\boldsymbol{v}$ is not guaranteed to be in L^2, therefore for any $\boldsymbol{u},\boldsymbol{v}\in H(\mathrm{div};\Omega)$ the inner product

$$\langle(\boldsymbol{a}\cdot\nabla)\boldsymbol{u},\boldsymbol{v}\rangle=\int_\Omega(\boldsymbol{a}\cdot\nabla)\boldsymbol{u}\cdot\boldsymbol{v}\,\mathrm{d}V \tag{4.1}$$

is not properly defined.

However, when the numerical approximation $\boldsymbol{u}_h$, which is represented by RT elements, is restricted to each triangular element $\mathcal{T}$, the components of $\boldsymbol{u}_h|_{\mathcal{T}}$ are polynomials and thus differentiable *within* $\mathcal{T}$. Hence, we consider

the integral (4.1) in an element-wise sense. Let Ω_h be a triangulation of the domain $\Omega \subset \mathbb{R}^N$. Then the integral involving the nonlinear advection term $\boldsymbol{N}(\boldsymbol{u})$ can then be approximated by

$$\langle \boldsymbol{N}(\boldsymbol{u}_h), \boldsymbol{v}_h \rangle_{\mathcal{T}} \coloneqq \sum_{\mathcal{T} \in \Omega_h} \int_{\mathcal{T}} \boldsymbol{N}(\boldsymbol{u}_h) \cdot \boldsymbol{v}_h \, \mathrm{d}V, \quad \forall \boldsymbol{v}_h \in RT_r(\Omega_h), \tag{4.2}$$

where $RT_r(\Omega_h)$ is the Raviart–Thomas finite element space that approximates $H(\mathrm{div}; \Omega_h)$, with $\nabla \boldsymbol{u}_h$ defined in each element $\mathcal{T} \in \Omega_h$.

The mixed FEM (MOL) spatial discretization of (2.5) and (2.6) are: Find $(\boldsymbol{\omega}_h, \boldsymbol{u}_h) \in \Sigma^h \times V^h$ such that $\boldsymbol{u}_h(t = 0) = \boldsymbol{u}_{0h}$ and

$$\langle \boldsymbol{\omega}_h, \boldsymbol{\tau}_h \rangle - \langle \boldsymbol{u}_h, \nabla \times \boldsymbol{\tau}_h \rangle = \int_{\partial\Omega} \boldsymbol{\tau}_h \cdot (\boldsymbol{n} \times \boldsymbol{g}) \, \mathrm{d}S \qquad \forall \boldsymbol{\tau}_h \in \Sigma^h, \tag{4.3a}$$

$$\langle (\boldsymbol{u}_h)_t, \boldsymbol{v}_h \rangle + \langle \boldsymbol{N}(\boldsymbol{u}_h), \boldsymbol{v}_h \rangle_{\mathcal{T}} = -\nu \langle \nabla \cdot \boldsymbol{u}_h, \nabla \cdot \boldsymbol{v}_h \rangle - \nu \langle \nabla \times \boldsymbol{\omega}_h, \boldsymbol{v}_h \rangle + \langle \boldsymbol{f} - \nabla P(\boldsymbol{u}_h), \boldsymbol{v}_h \rangle \quad \forall \boldsymbol{v}_h \in V^h, \tag{4.3b}$$

and

$$\begin{aligned} \langle \nabla p_h, \nabla q_h \rangle = \langle \boldsymbol{f}, \nabla q_h \rangle - \langle \boldsymbol{N}(\boldsymbol{u}_h), \boldsymbol{v}_h \rangle_{\mathcal{T}} - \nu \int_{\partial\Omega} \boldsymbol{n} \cdot (\nabla \times \boldsymbol{\omega}) q_h \, \mathrm{d}S \\ + \lambda \int_{\partial\Omega} \boldsymbol{n} \cdot (\boldsymbol{u} - \boldsymbol{g}) q_h \, \mathrm{d}S - \int_{\partial\Omega} (\boldsymbol{n} \cdot \boldsymbol{g}_t) q_h \, \mathrm{d}S, \quad \forall q_h \in P_r. \end{aligned} \tag{4.4}$$

where for $N = 2$, $\Sigma^h \times V^h = P_r \times RT_{r-1}$ with a triangular mesh, and for $N = 3$, $\Sigma^h \times V^h = NED_r^1 \times RT_{r-1}$ with a tetrahedral mesh.

The following full numerical scheme closely parallels Numerical Scheme 1, with the key difference being the inclusion of the nonlinear term:

Numerical Scheme 2. *Navier–Stokes PPE equation (rth order in space, 3rd order in time).*

1. *Method of lines (MOL) spatial discretization yields an ODE IVP: (4.3)–(4.4).*
2. *Time-discretize (4.3)–(4.4) via 3rd order IMEX (4,4,3) (with coefficients in (3.22)). In the IMEX scheme steps (3.11), the implicit and explicit parts are given by:*

$$\begin{aligned} \mathcal{G}(u^n) &\leftarrow -\nu \langle \nabla \cdot \boldsymbol{u}_h, \nabla \cdot \boldsymbol{v}_h \rangle - \nu \langle \nabla \times \boldsymbol{\omega}_h, \boldsymbol{v}_h \rangle, \\ \mathcal{F}(u^n) &\leftarrow \langle \boldsymbol{f} - \nabla P(\boldsymbol{u}_h), \boldsymbol{v}_h \rangle - \langle \boldsymbol{N}(\boldsymbol{u}_h), \boldsymbol{v}_h \rangle_{\mathcal{T}}. \end{aligned}$$

3. *Time-advance the full space–time discretized scheme. At each RK stage time-step, the mixed FEM variables $(\boldsymbol{\omega}_h, \boldsymbol{u}_h)$ solve a saddle-point system; and the pressure variables p_h solve a linear system.*

4.2. Numerical results on manufactured solutions

In this subsection, we present convergence results for the full scheme: PPE reformulation with the nonlinear advection term treated as described in the previous subsection. To test the treatment of the advection term without the complications from the PPE reformulation, we first study the spatial convergence of the mixed formulation applied to the vector advection–diffusion equation with electric boundary conditions. We then present the convergence results for the full problem with the nonlinear term.

4.2.1. Nonlinear vector advection–diffusion equation with EBC

To study the performance of the proposed treatment (4.2) of the advection term, we consider the same semi-periodic domain and manufactured solution as in Section 3.4.1, but for the vector-valued nonlinear advection–diffusion equation:

$$\boldsymbol{u}_t + (\boldsymbol{u} \cdot \nabla)\boldsymbol{u} = \Delta \boldsymbol{u} + \boldsymbol{f} \qquad \text{for } (x, y) \in (0, 1)^2, \tag{4.5}$$

$$\boldsymbol{n} \times \boldsymbol{u} = 0, \quad \nabla \cdot \boldsymbol{u} = 0 \qquad \text{for } (x, y) \in [0, 1) \times \{0, 1\}, \tag{4.6}$$

$$\boldsymbol{u}(0, y) = \boldsymbol{u}(1, y) \qquad \text{for } 0 < y < 1. \tag{4.7}$$

Table 5
Observed spatial convergence rates in the L^2 norm for the vector nonlinear advection–diffusion equation with electric boundary conditions (4.5)–(4.7). The spatial approximation orders are $r = 1, 2, 3, 4, 5$.

Spatial approximation order $r = 1$, $(\boldsymbol{\omega}_h, \boldsymbol{u}_h, p_h) \in P_1 \times RT_0 \times P_1$										
Δx	$\boldsymbol{u}$	Rate	$\nabla \cdot \boldsymbol{u}$	Rate	$\nabla \boldsymbol{u}$	Rate	$\boldsymbol{\omega}$	Rate	$\nabla \times \boldsymbol{\omega}$	Rate
2.50E−01	6.93E+00	—	1.00E+01	—	1.37E+02	—	1.37E+02	—	2.76E+03	—
1.25E−01	3.28E+00	1.08	5.92E+00	0.76	1.37E+02	0.00	3.19E+01	2.10	1.45E+03	0.92
6.25E−02	1.67E+00	0.97	2.36E+00	1.33	1.37E+02	0.00	7.60E+00	2.07	7.25E+02	1.00
3.13E−02	8.75E−01	0.94	2.24E+00	0.07	1.37E+02	0.00	2.82E+00	1.43	3.65E+02	0.99
1.56E−02	5.07E−01	0.79	2.27E+00	−0.02	1.37E+02	−0.00	2.30E+00	0.30	1.87E+02	0.97
7.81E−03	3.60E−01	0.49	2.28E+00	−0.01	1.37E+02	−0.00	2.27E+00	0.02	1.01E+02	0.88
Spatial approximation order $r = 2$, $(\boldsymbol{\omega}_h, \boldsymbol{u}_h, p_h) \in P_2 \times RT_1 \times P_2$										
Δx	$\boldsymbol{u}$	Rate	$\nabla \cdot \boldsymbol{u}$	Rate	$\nabla \boldsymbol{u}$	Rate	$\boldsymbol{\omega}$	Rate	$\nabla \times \boldsymbol{\omega}$	Rate
2.50E−01	2.13E+00	—	9.11E+00	—	9.33E+01	—	2.47E+01	—	1.25E+03	—
1.25E−01	7.92E−01	1.43	1.77E+00	2.37	6.26E+01	0.58	7.62E+00	1.70	4.03E+02	1.64
6.25E−02	2.14E−01	1.89	4.20E−01	2.07	3.28E+01	0.93	2.07E+00	1.88	1.17E+02	1.79
3.13E−02	5.48E−02	1.97	8.91E−02	2.24	1.66E+01	0.98	5.23E−01	1.98	3.92E+01	1.57
1.56E−02	1.38E−02	1.99	2.10E−02	2.08	8.33E+00	0.99	1.31E−01	2.00	1.63E+01	1.27
7.81E−03	3.45E−03	2.00	5.18E−03	2.02	4.17E+00	1.00	3.27E−02	2.00	7.65E+00	1.09
Spatial approximation order $r = 3$, $(\boldsymbol{\omega}_h, \boldsymbol{u}_h, p_h) \in P_3 \times RT_2 \times P_3$										
Δx	$\boldsymbol{u}$	Rate	$\nabla \cdot \boldsymbol{u}$	Rate	$\nabla \boldsymbol{u}$	Rate	$\boldsymbol{\omega}$	Rate	$\nabla \times \boldsymbol{\omega}$	Rate
2.50E−01	1.33E+00	—	3.90E+00	—	7.10E+01	—	1.90E+01	—	6.41E+02	—
1.25E−01	1.28E−01	3.37	3.47E−01	3.49	1.67E+01	2.09	1.32E+00	3.85	8.12E+01	2.98
6.25E−02	1.58E−02	3.02	4.27E−02	3.02	4.24E+00	1.98	1.00E−01	3.72	1.16E+01	2.80
3.13E−02	2.03E−03	2.96	6.82E−03	2.65	1.06E+00	2.00	1.13E−02	3.16	2.25E+00	2.37
1.56E−02	2.90E−04	2.81	1.43E−03	2.25	2.66E−01	2.00	2.06E−03	2.45	5.15E−01	2.13
Spatial approximation order $r = 4$, $(\boldsymbol{\omega}_h, \boldsymbol{u}_h, p_h) \in P_4 \times RT_3 \times P_4$										
Δx	$\boldsymbol{u}$	Rate	$\nabla \cdot \boldsymbol{u}$	Rate	$\nabla \boldsymbol{u}$	Rate	$\boldsymbol{\omega}$	Rate	$\nabla \times \boldsymbol{\omega}$	Rate
2.50E−01	2.42E−01	—	1.72E+00	—	1.94E+01	—	2.71E+00	—	1.57E+02	—
1.25E−01	1.74E−02	3.80	7.45E−02	4.53	3.03E+00	2.68	1.80E−01	3.91	1.16E+01	3.76
6.25E−02	1.20E−03	3.86	2.53E−03	4.88	4.04E−01	2.91	1.40E−02	3.68	1.09E+00	3.41
3.13E−02	7.74E−05	3.96	1.33E−04	4.25	5.14E−02	2.97	9.28E−04	3.92	1.16E−01	3.22
1.56E−02	4.88E−06	3.99	7.79E−06	4.09	6.46E−03	2.99	5.89E−05	3.98	1.38E−02	3.07
Spatial approximation order $r = 5$, $(\boldsymbol{\omega}_h, \boldsymbol{u}_h, p_h) \in P_5 \times RT_4 \times P_4$										
Δx	$\boldsymbol{u}$	Rate	$\nabla \cdot \boldsymbol{u}$	Rate	$\nabla \boldsymbol{u}$	Rate	$\boldsymbol{\omega}$	Rate	$\nabla \times \boldsymbol{\omega}$	Rate
2.50E−01	8.59E−02	—	4.32E−01	—	6.56E+00	—	1.28E+00	—	4.61E+01	—
1.25E−01	2.17E−03	5.31	8.36E−03	5.69	4.81E−01	3.77	2.93E−02	5.45	1.82E+00	4.66
6.25E−02	6.37E−05	5.09	1.74E−04	5.59	3.14E−02	3.94	5.27E−04	5.80	7.55E−02	4.59
3.13E−02	1.99E−06	5.00	7.18E−06	4.60	1.98E−03	3.99	1.28E−05	5.36	4.10E−03	4.20
1.56E−02	6.80E−08	4.87	3.68E−07	4.29	1.24E−04	4.00	5.41E−07	4.57	2.46E−04	4.06

In the presence of the nonlinear advection term, systematic degradations in the spatial convergence order are observed (see Table 5). Specifically, non-convergent result is observed for $r = 1$. For $r = 2, 4$, the convergence rates are r, r, $r - 1$, r and $r - 1$ for $\boldsymbol{u}$, $\nabla \cdot \boldsymbol{u}$, $\nabla \boldsymbol{u}$, $\boldsymbol{\omega}$ and $\nabla \times \boldsymbol{\omega}$, respectively (in both the L^2 and L^∞ norms). The convergence rates are less clean when r is odd, but follow a similar pattern as in the even order case. These results indicate that degradation in the convergence order for the full PPE reformulation (2.5)–(2.6) should be expected.

4.2.2. The PPE reformulation (2.5)–(2.6) (including the nonlinear advection term)

Consider the same manufactured solution, defined on the unit square $\Omega = [0, 1]^2$, as in Section 3.4.4. However, since here we solve the full problem (2.5)–(2.6), the forcing function is given by $\boldsymbol{f} = \boldsymbol{u}_t + (\boldsymbol{u} \cdot \nabla)\boldsymbol{u} - \nu \Delta \boldsymbol{u} + \nabla p$. We then use: the 3rd order spatial discretization $(\boldsymbol{\omega}_h, \boldsymbol{u}_h, p_h) \in P_3 \times RT_2 \times P_3$, the 3rd order IMEX(4,4,3) with time step $\Delta t = 0.2\Delta x$, the final time $T = 3$, and $\lambda = 30$ (the same as in the previous test cases).

The error convergence is shown in Table 6 in the L^2 norm (top) and in the L^∞ norm (bottom). Convergent results are observed for all quantities but with slightly degraded convergence rates in comparison to the linear case in Table 4. In particular, the convergence rate for $\nabla \cdot \boldsymbol{u}$ is a little bigger than 3 as opposed to 4 in the linear case, and $\nabla \times \boldsymbol{\omega}$, p and ∇p show a 2nd order convergence.

4.3. Numerical results on benchmark tests

In this subsection, we demonstrate the performance of the proposed method for solving several benchmark problems: a Taylor–Green vortex flow in Section 4.3.1, lid-driven cavity in Section 4.3.2, and flow over a backward-facing step in Section 4.3.3. We conclude the subsection with a 3D Couette–Poiseuille flow in a cylindrical pipe. The results show good agreement with known exact solutions or reference data.

Table 6
Error convergence for the full Navier–Stokes problem (including the nonlinear advection term) in the L^2 norm (top) and the L^∞ norm (bottom). The problem is solved with the 3rd order time-stepping IMEX(4,4,3), the 3rd order spatial discretization $P_3 \times RT_2 \times P_3$, the final time $T = 3$, and $\lambda = 30$.

Error convergence in L^2 norm													
Δx	$\boldsymbol{u}$		$\nabla \cdot \boldsymbol{u}$		$\nabla \boldsymbol{u}$		$\boldsymbol{\omega}$		$\nabla \times \boldsymbol{\omega}$		p		∇p	
2.50E−01	4.28E−02	—	1.02E−01	—	2.92E+00	—	3.37E−01	—	1.47E+01	—	2.60E−01	—	5.70E+00	—
1.25E−01	8.14E−03	2.40	9.39E−03	3.45	1.03E+00	1.51	3.52E−02	3.26	2.97E+00	2.30	5.33E−02	2.28	9.49E−01	2.59
6.25E−02	1.05E−03	2.96	7.22E−04	3.70	2.62E−01	1.97	4.74E−03	2.89	5.93E−01	2.33	1.45E−02	1.87	2.42E−01	1.97
3.13E−02	1.36E−04	2.95	5.89E−05	3.62	6.57E−02	2.00	8.15E−04	2.54	1.37E−01	2.12	3.69E−03	1.98	6.11E−02	1.99
1.56E−02	1.84E−05	2.88	5.91E−06	3.32	1.64E−02	2.00	1.64E−04	2.31	3.34E−02	2.03	9.18E−04	2.01	1.52E−02	2.01
7.81E−03	2.70E−06	2.77	6.84E−07	3.11	5.64E−03	1.54	3.68E−05	2.16	8.30E−03	2.01	2.28E−04	2.01	3.82E−03	1.99
Error convergence in L^∞ norm														
Δx	$\boldsymbol{u}$		$\nabla \cdot \boldsymbol{u}$		$\nabla \boldsymbol{u}$		$\boldsymbol{\omega}$		$\nabla \times \boldsymbol{\omega}$		p		∇p	
2.50E−01	2.37E−01	—	3.20E−01	—	1.30E+01	—	2.32E+00	—	1.05E+02	—	1.24E+00	—	2.87E+01	—
1.25E−01	1.12E−01	1.09	7.30E−02	2.13	7.80E+00	0.74	2.31E−01	3.33	2.30E+01	2.19	3.51E−01	1.83	5.27E+00	2.45
6.25E−02	1.77E−02	2.65	5.69E−03	3.68	2.12E+00	1.88	3.58E−02	2.69	3.97E+00	2.54	9.41E−02	1.90	1.89E+00	1.48
3.13E−02	2.34E−03	2.92	3.56E−04	4.00	5.36E−01	1.98	4.99E−03	2.85	9.46E−01	2.07	2.34E−02	2.01	5.60E−01	1.76
1.56E−02	2.97E−04	2.98	2.98E−05	3.58	1.34E−01	2.00	7.17E−04	2.80	2.38E−01	1.99	5.78E−03	2.02	1.47E−01	1.93
7.81E−03	3.73E−05	2.99	3.15E−06	3.24	3.35E−02	2.00	1.46E−04	2.29	6.02E−02	1.98	1.43E−03	2.01	3.73E−02	1.97

Table 7
Error convergence in the L^2 norm and in the L^∞ norm for the Taylor–Green vortex problem. The problem is solved with the 3rd order spatial approximation $P_3 \times RT_2 \times P_3$ and the 3rd order IMEX(4,4,3) time-stepping scheme.

Δx	$\boldsymbol{u}$ (L^2/L^∞)	Rate	$\nabla \cdot \boldsymbol{u}$ (L^2/L^∞)	Rate	$\boldsymbol{\omega}$ (L^2/L^∞)	Rate	p (L^2/L^∞)	Rate
1.25E−01	1.56E−03/2.31E−03	— /—	1.09E−04/2.68E−04	— /—	2.73E−02/5.43E−02	— / —	3.73E−05/6.73E−05	—/—
6.25E−02	2.33E−04/3.51E−04	2.75/2.72	1.93E−06/5.66E−06	5.82/5.57	4.08E−03/8.37E−03	2.74/2.70	3.52E−06/7.40E−06	3.41/3.18
3.12E−02	3.23E−05/5.08E−05	2.85/2.79	2.14E−07/1.06E−06	3.17/2.41	5.68E−04/1.15E−03	2.84/2.86	9.15E−08/2.81E−07	5.27/4.72
1.56E−02	3.80E−06/6.50E−06	3.09/2.97	2.37E−08/8.50E−08	3.17/3.65	6.67E−05/1.34E−04	3.09/3.10	1.15E−07/ 2.53E−07	−0.33/0.15
7.81E−03	4.62E−07/8.19E−07	3.04/2.99	2.78E−09/1.08E−08	3.09/2.97	8.09E−06/1.62E−05	3.04/3.05	4.33E−08/9.19E−08	1.41/1.46
3.91E−03	5.86E−08/1.04E−07	2.98/2.97	3.44E−10/1.37E−09	3.02/2.98	1.03E−06/2.06E−06	2.98/2.98	1.25E−08/2.63E−08	1.79/1.80

4.3.1. Taylor–Green vortex problem

We consider the Taylor–Green vortex problem in a unit square domain $\Omega = [0, 1]^2$ with periodic boundary conditions in both directions. The exact solution is

$$u(x, y, t) = \exp(-2k^2\nu t)\sin(kx)\cos(ky),$$
$$v(x, y, t) = -\exp(-2k^2\nu t)\cos(kx)\sin(ky),$$
$$p(x, y, t) = \frac{1}{4}\exp(-4k^2\nu t)(\cos(2kx) + \cos(2ky)).$$

We choose the parameters $k = 4\pi$, $\nu = 0.05$ and a final time $T = 0.2$, the same as in [44]. The time step is taken as $\Delta t = 0.5\Delta x$. We solve this problem with the 3rd order spatial approximation $(\boldsymbol{\omega}_h, \boldsymbol{u}_h, p_h) \in P_3 \times RT_2 \times P_3$ and the 3rd order IMEX(4,4,3). The error convergence is shown in Table 7 in the L^2 norm and in the L^∞ norm. The observed convergence rates for $\boldsymbol{u}$, $\nabla \cdot \boldsymbol{u}$ and $\boldsymbol{\omega}$ are 3. The pressure shows a convergence rate that is slightly less than 2. Fig. 4 shows the computed velocity component u and the pressure at the final time on the mesh with $\Delta x = 3.91 \times 10^{-3}$.

4.3.2. Lid-driven cavity

For the lid-driven cavity, we compute the flow in the unit square domain $[0, 1]^2$, with $\lambda = 10$, using the 3rd order spatial approximation $P_3 \times RT_2 \times P_3$ and 3rd order IMEX RK time-stepping (time step $\Delta t = 0.8\Delta x$), on a regular triangular mesh with 16 384 elements and a mesh size $\Delta x = 1.5625 \times 10^{-2}$. The velocity field is advanced forward in time until it reaches steady state, for Reynolds numbers 100, 400 and 1000. The flow starts at rest, with boundary conditions $\boldsymbol{g} = (1, 0)^T$ at the top wall and no-slip elsewhere.

The results for $Re = 100$, 400 and 1000 are shown in Figs. 5–7. The streamlines for the steady state flow are shown in the left panel of each figure.[1] The velocity profiles along the centerlines of the cavity (i.e. $u(0.5, y)$ and $v(x, 0.5)$) are plotted in the right panel, together with the reference data from [75]. Note that some streamlines in the plots end at the domain boundary, without forming closed curves. This is due to the following facts: (i) the numerical

[1] The streamlines at the final time, T, are computed by numerically solving the ODE $\frac{d\boldsymbol{x}}{ds} = \boldsymbol{u}(\boldsymbol{x}, T)$ with an explicit 4th order Runge–Kutta (RK4) scheme.

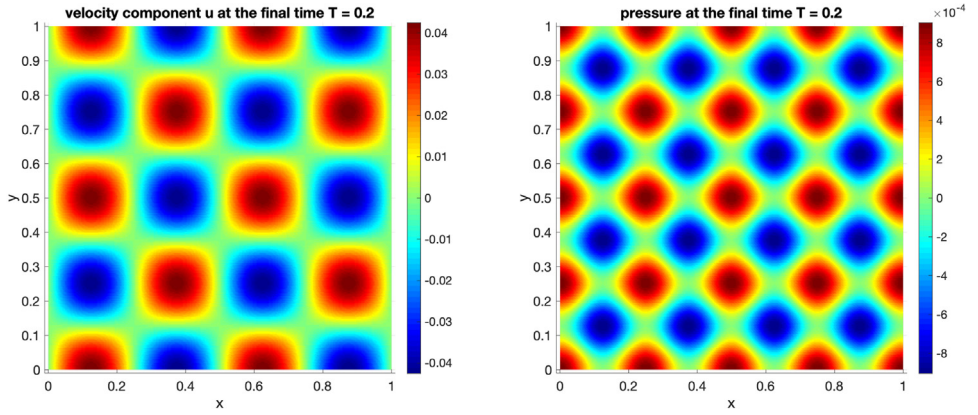

Fig. 4. Numerical solution of the Taylor–Green Vortex problem at the final time $T = 0.2$. Left: first component of the velocity $\boldsymbol{u}_h$. Right: pressure p_h.

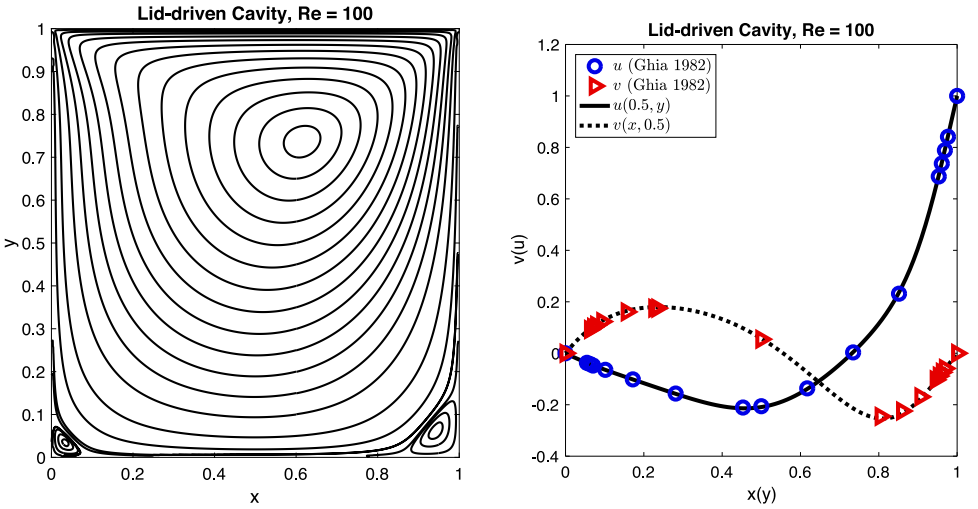

Fig. 5. Lid-driven cavity flow with $Re = 100$. Left: Streamlines at steady state. Right: Velocity profiles along the centerlines (solid line: $u(0.5,\ y)$, and dashed line: $v(x,\ 0.5)$) compared with the reference data (blue circles and red triangles) in [75].

solution is not exactly divergence-free, (ii) the normal velocity condition at the boundary is not enforced strongly (in the Dirichlet sense) but rather through the ODE (2.8), which results in a small (as small as the resolution) flow through the boundary.

The flow through the boundary is more pronounced at the top corners, where discontinuities in the velocity occurs. Increasing λ makes the enforcing of the normal velocity condition stronger (see Section 3.4.5), and reduces the flow through the boundary. However, making λ too big would impose an undesirable time step restriction, $\Delta t < O(\frac{1}{\lambda})$, through the relaxation term in (2.8).

4.3.3. Backward-facing step

In this test case, we compute the benchmark problem of flow over a backward-facing step for $Re = 100$ and $Re = 200$. Again, we use the 3rd order spatial discretization $P_3 \times RT_2 \times P_3$, a 3rd order IMEX RK scheme and $\lambda = 10$. The computation uses a non-uniform triangular mesh with extra mesh refinement near the reentrant corner and the region behind the step. The minimum mesh size is $\Delta x = 1.7028 \times 10^{-2}$ and the time step is set to $\Delta t = 0.02\Delta x$. In this case the domain of computation is

$$\Omega = [0, L] \times [-0.5, 0.5] \backslash [0, 0.5] \times [-0.5, 0],$$

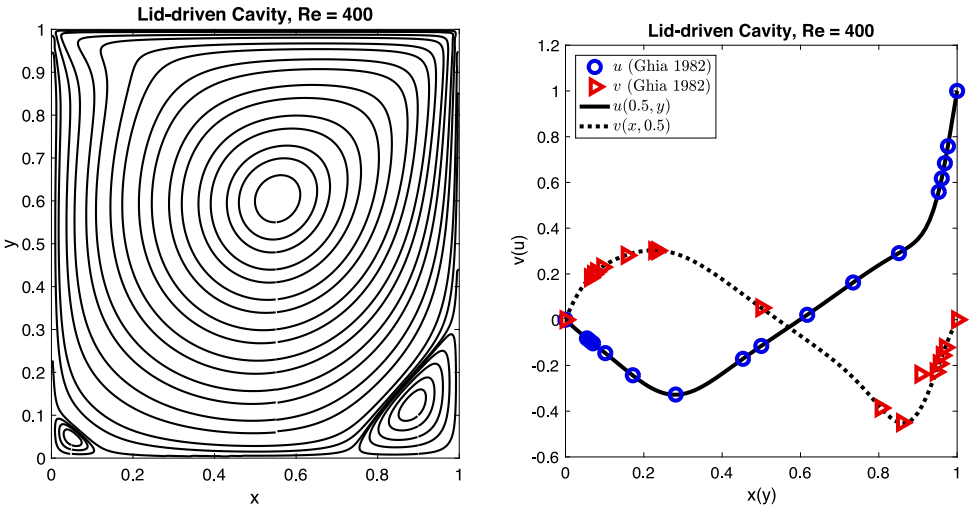

Fig. 6. Lid-driven cavity flow with $Re = 400$. Left: Streamlines at steady state. Right: Velocity profiles along the centerlines (solid line: $u(0.5,\ y)$, and dashed line: $v(x,\ 0.5)$) compared with the reference data (blue circles and red triangles) in [75].

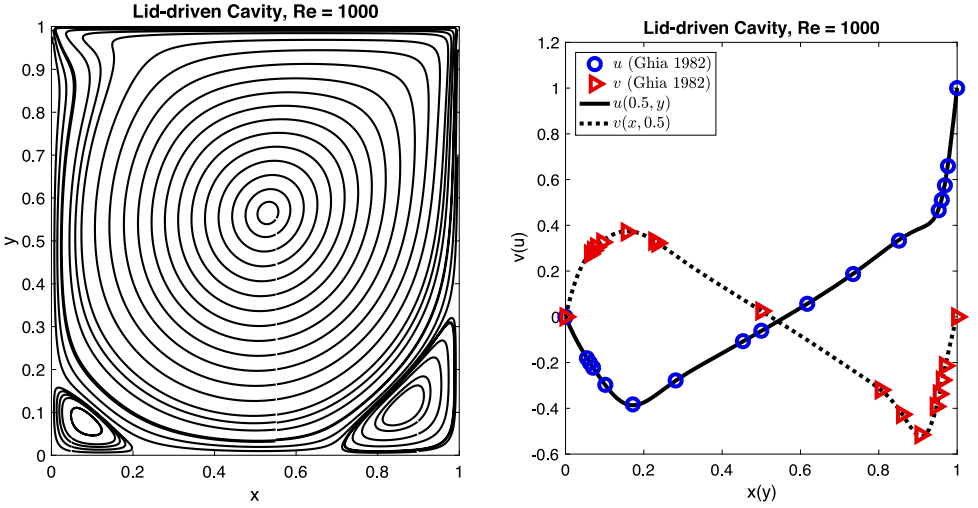

Fig. 7. Lid-driven cavity flow with $Re = 1000$. Left: Streamlines at steady state. Right: Velocity profiles along the centerlines (solid line: $u(0.5,\ y)$, and dashed line: $v(x,\ 0.5)$) compared with the reference data (blue circles and red triangles) in [75].

where L is the channel length, set to $L = 8$. No-slip boundary conditions are imposed everywhere, except for the inflow and outflow boundaries at $x = 0$ and $x = L$. The inflow and outflow boundary conditions are

$$\boldsymbol{g}_{\text{inflow}} = f(t)\,(12y(1-2y), 0)^T\,,$$
$$\boldsymbol{g}_{\text{outflow}} = f(t)\left(-3y^2 + \frac{3}{4}, 0\right)^T\,,$$

where $f(t) = 1 - e^{-6t^2}$, so that the flow is initially at rest and the inflow and outflow increase gradually with time. The mean inflow velocity U reaches 1 for large enough t. We use the channel height $H = 1$ as the characteristic length, which gives a Reynolds number $Re = HU/\nu = 1/\nu$.

For $Re = 100$ and 200, the only recirculating flow forms behind the step. More regions of recirculating flow appear down the channel as the Reynolds number increases. The streamlines shown in Fig. 8 were computed using the same procedure described in Section 4.3.2.

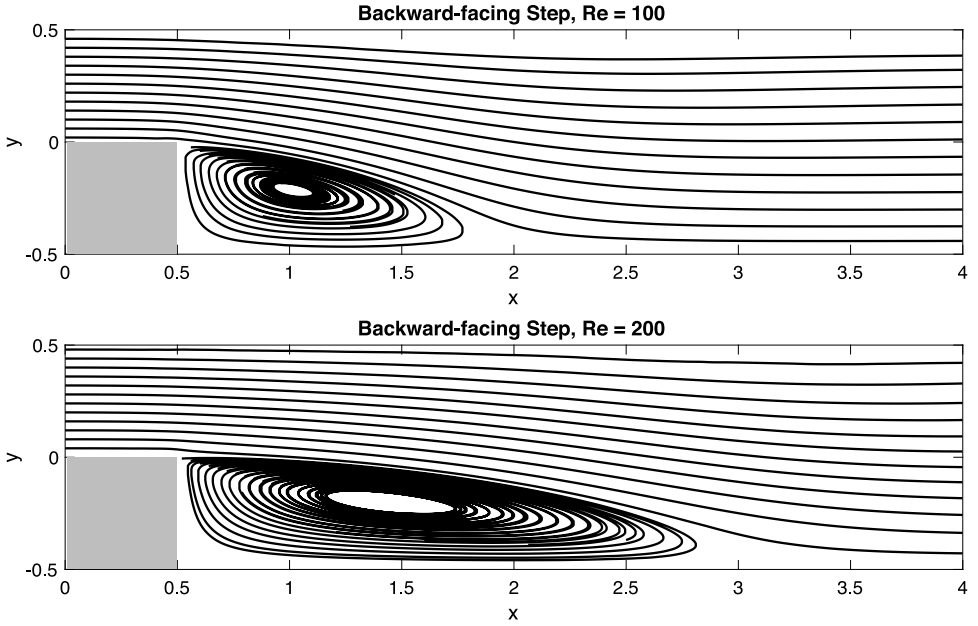

Fig. 8. Streamlines for the computation of a flow over a backward-facing step, at steady state, for $Re = 100$ (top) and $Re = 200$ (bottom).

To compare our results with the reference data in [76] we use the position of the reattachment point, where the line separating the recirculating flow behind the step and the main flow in the channel meets the channel wall, i.e. the domain boundary. For this purpose introduce the nondimensional ratio L_1/S, where L_1 is the distance between the foot of the step and the reattachment point, and $S = 0.5$ is the step height. For $Re = 100$, the ratio $L_1/S = 2.96$ in our computation compares well with the reference data ratio: 2.922. For $Re = 200$, our computation yields a ratio $L_1/S = 4.86$, while the reference value is 4.982. Our results show a rather good agreement with the reference values.

4.3.4. 3D Couette-Poiseuille flow in a cylindrical pipe

We consider the Couette–Poiseuille flow in a periodic cylindrical pipe [44] with length 0.5, radius $R = 1$ and periodic boundary conditions in the axial direction. The exact solution in cylindrical coordinates is

$$\boldsymbol{u} = u_1 \boldsymbol{e}_x + u_r \boldsymbol{e}_r + u_\theta \boldsymbol{e}_\theta, \quad p(r,t) = \int_0^r (u_\theta(\bar{r}))^2 \frac{1}{\bar{r}} d\bar{r} + C,$$

where

$$u_1 = \frac{G}{2\nu}(R^2 - r^2) + \alpha_0 J_0(\lambda_0 r) e^{-\lambda_0^2 \nu t}, \quad u_r = 0, \quad u_\theta = \omega r + \alpha_1 J_1(\lambda_1 r) e^{-\lambda_1^2 \nu t}.$$

The vectors $\boldsymbol{e}_x$, $\boldsymbol{e}_r$ and $\boldsymbol{e}_\theta$ denote unit vectors in the axial, the radial and the angular directions respectively. The flow is driven by a constant body force $\boldsymbol{f} = (2G, 0, 0)^T$. In Cartesian coordinates, the exact solution becomes

$$\boldsymbol{u} = u\boldsymbol{e}_x + v\boldsymbol{e}_y + w\boldsymbol{e}_z,$$

where

$$u = \frac{G}{2\nu}(R^2 - y^2 - z^2) + \alpha_0 J_0(\lambda_0 \sqrt{y^2 + z^2}) e^{-\lambda_0^2 \nu t},$$
$$v = -\omega z - \alpha_1 \frac{z}{\sqrt{y^2 + z^2}} J_1(\lambda_1 \sqrt{y^2 + z^2}) e^{-\lambda_1^2 \nu t},$$
$$w = \omega y + \alpha_1 \frac{y}{\sqrt{y^2 + z^2}} J_1(\lambda_1 \sqrt{y^2 + z^2}) e^{-\lambda_1^2 \nu t}.$$

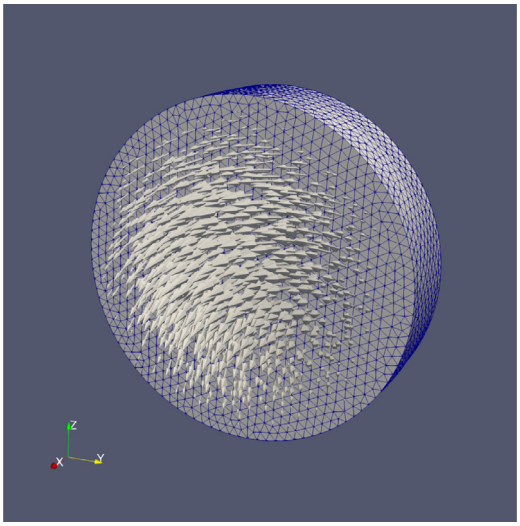

Fig. 9. A sample mesh of the cylindrical pipe, with arrows indicating the computed velocity field.

Table 8
Error convergence in the L^2 norm and in the L^∞ norm for the 3D Couette–Poiseuille flow in a cylindrical pipe. The problem is solved with the 3rd order spatial approximation and the 3rd order IMEX(4,4,3) time-stepping scheme.

Δx	$\boldsymbol{u}$ (L^2/L^∞)	Rate	$\nabla\cdot\boldsymbol{u}$ (L^2/L^∞)	Rate	$\boldsymbol{\omega}$ (L^2/L^∞)	Rate	∇p (L^2/L^∞)	Rate
7.64E−01	1.41E−02/6.42E−02	— /—	2.76E−02/1.01E−01	— /—	9.79E−02/3.47E−01	— /—	6.77E−02/2.14E−01	— /—
3.90E−01	1.97E−03/1.32E−02	2.92/2.35	1.71E−03/8.53E−03	4.14/3.68	1.08E−02/3.73E−02	3.28/3.31	1.06E−02/5.76E−02	2.76/1.95
2.24E−01	8.42E−04/7.63E−03	1.53/0.99	6.01E−04/2.88E−03	1.88/1.95	4.44E−03/2.38E−02	1.60/0.81	4.98E−03/2.28E−02	1.36/1.67
1.21E−01	1.49E−04/2.15E−03	2.80/2.05	9.72E−05/9.56E−04	2.95/1.79	7.93E−04/7.93E−03	2.79/1.78	1.53E−03/7.21E−03	1.91/1.86
6.04E−02	1.85E−05/2.36E−04	3.02/3.19	1.21E−05/1.49E−04	3.00/2.69	1.09E−04/1.88E−03	2.87/2.08	3.97E−04/1.81E−03	1.95/1.99

Note that $v = w = 0$ when $y^2 + z^2 = 0$. Here $\lambda_0 = 2.4048255577$ and $\lambda_1 = 3.8317059702$ are the smallest positive roots of Bessel functions J_0 and J_1, respectively. For the computation, we set $G = 0.2$, $\omega = 0$, $\nu = 0.1$, and $\alpha_0 = \alpha_1 = 1$. The problem is solved with the 3rd order spatial approximation and the 3rd order IMEX(4,4,3) with a stabilizing parameter $\lambda = 10$, a final time $T = 0.1$ and time step $\Delta t = 0.1\Delta x$. Note that Nédélec elements are used to approximate $\boldsymbol{\omega}$ in 3D.

Fig. 9 shows a sample mesh of the cylindrical pipe together with the computed velocity field of flow coming out of the cylinder bottom wall. The convergence results in the L^2 norm and in the L^∞ norm are shown in Table 8. The velocity $\boldsymbol{u}$ is observed to have a convergence rate around 3 in both norms. The pressure gradient is 2nd order convergent in both norms. For the divergence and the curl, convergence rates are at least 2 in both norms with the L^2 norm rates around 3.

5. Conclusions and outlook

We investigated finite element formulations for a PPE reformulation of the incompressible Navier–Stokes equations. In the PPE reformulation, the momentum equation is in the form of a vector heat equation with electric boundary conditions, and the pressure appears as a global function of the velocity (obtained, at any time, as the solution to a Poisson equation). Thus this reformulation allows for high-order time-stepping via standard schemes. In particular, the decoupling of the velocity and the pressure can be achieved by IMEX time-stepping schemes, and modern high-order IMEX schemes can be applied in a straightforward manner.

We demonstrated via numerical examples that our proposed numerical schemes, based on the PPE reformulation (2.5)–(2.6), have the potential to achieve high-order both in space and in time, while avoiding severe time step restrictions. The methods have important advantages:

(i) The use of an IMEX time-stepping strategy decouples the velocity and the pressure in the numerical methods, and at the same time avoids diffusive time step restrictions.

(ii) The methods can achieve high-order in time with off-the-shelf high-order IMEX RK schemes. Therefore the code can be easily adapted to newly developed IMEX schemes with better properties, for instance, unconditional stability, order reduction avoidance, etc. A natural future research direction includes developing new IMEX RK time-stepping schemes for the PPE reformulations with such properties.

(iii) Standard mixed finite element formulations of incompressible fluid flow problems (Stokes and Navier–Stokes equations) require the velocity and pressure approximations to satisfy the inf–sup condition for stability, which limits the choices of finite element approximations. Our new schemes allow for more flexible choices of finite element spaces for the velocity and pressure, avoiding the inf–sup condition.

Note also that an interesting feature of the methods studied in this paper is that the quantity $\nabla \cdot \boldsymbol{u}$ converges to zero at an additional order relative to the accuracy of the velocity field itself. As a consequence, for well-resolved computations, the methodology will generally yield velocity fields that are extremely close to divergence-free, even though no discrete incompressibility principle needs to be imposed.

Despite the important advantages mentioned above, the methods also have some limitations:

(i) The discretization of the (nonlinear) advection term does not fit into the finite element formulation due to the discontinuities across elements in the tangential velocity. The current approach leads to convergent methods but results in degradations in the error convergence rates.

(ii) The mixed formulation for the velocity deals with the EBC naturally. However, it introduces a saddle point problem. Therefore the choices for the FE approximations for $\boldsymbol{u}$ and $\boldsymbol{\omega}$ need to satisfy the inf–sup condition. The mixed formulation also increases the degrees of freedom of the discrete problem, as the new variable $\boldsymbol{\omega} = \nabla \times \boldsymbol{u}$ is introduced.

As a final comment, the IMEX schemes here provide a stable explicit treatment of the pressure and implicit treatment of viscosity. As is common in (nonlinear) advection equations, explicit treatments of the advection term $\boldsymbol{u} \cdot \nabla \boldsymbol{u}$ become destabilizing with increasing Reynolds number. Hence, for higher RE flows, additional stabilization techniques, such as streamline upwind Petrov–Galerkin, will be required.

Declaration of competing interest

The authors declare that they have no known competing financial interests or personal relationships that could have appeared to influence the work reported in this paper.

Acknowledgments

The authors wish to acknowledge support by the National Science Foundation, United States of America through the grants DMS-1719637 and DMS-1614043 (Rosales), DMS-1719640 (Seibold and Zhou), DMS-2012271 (Seibold), and DMS-1719693 and DMS-2012268 (Shirokoff).

This research includes calculations carried out on HPC resources supported in part by the National Science Foundation, United States of America through major research instrumentation grant number 1625061 and by the US Army Research Laboratory under contract number W911NF-16-2-0189.

Appendix. Discrete solvability of the Poisson equation

The pressure Poisson problem considered here in (3.2) has pure Neumann boundary conditions prescribed, hence it is solvable only if a compatibility condition is satisfied (see Remark 2.1), and the solution is unique only up to an additive constant. Note however, in practice other boundary conditions involving the pressure (such as a mixed boundary condition) may result in cases where the pressure equation does not require a solvability condition and is unique. The pressure Poisson problem (3.2) has pure Neumann boundary conditions prescribed, hence it is solvable only if a compatibility condition is satisfied (see Remark 2.1), and the solution is unique only up to an additive constant. In order to single out a unique solution, and at the same time to obtain a stable approximate solution in case the compatibility condition is not exactly satisfied (due to approximation errors), we employ the following standard least-squares approximation procedure. First, we impose an extra zero-mean constraint on the pressure:

$$\int_{\Omega} p \, \mathrm{d}V = 0.$$

This gives rise to an augmented system for the pressure with an additional scalar variable representing the Lagrange multiplier for the zero-mean constraint. For simplicity, the presentation here is carried out for homogeneous boundary conditions $\boldsymbol{g} = 0$. The weak formulation then becomes: Find $p \in H^1(\Omega)$ and $c \in \mathbb{R}$ s.t.

$$\langle \nabla p, \nabla q \rangle + \langle c, q \rangle = \langle \boldsymbol{f}, \nabla q \rangle - \nu \int_{\partial\Omega} \boldsymbol{n} \cdot (\nabla \times \boldsymbol{\omega}) q \, \mathrm{d}S + \lambda \int_{\partial\Omega} (\boldsymbol{n} \cdot \boldsymbol{u}) q \, \mathrm{d}S \quad \forall q \in H^1(\Omega), \tag{A.1a}$$

$$\langle p, d \rangle = 0 \qquad \forall d \in \mathbb{R}. \tag{A.1b}$$

Using standard nodal-based finite elements yields a linear system of the form

$$\begin{pmatrix} K & \boldsymbol{r} \\ \boldsymbol{r}^T & 0 \end{pmatrix} \cdot \begin{pmatrix} \boldsymbol{P} \\ c \end{pmatrix} = \begin{pmatrix} \boldsymbol{F} \\ 0 \end{pmatrix}. \tag{A.2}$$

Here K is the (symmetric) stiffness matrix of the FEM discretization of the Laplacian operator, $\boldsymbol{r}$ is the vector corresponding to constant functions (the null-vector of K), $\boldsymbol{P}$ is the solution vector for the pressure p, and c is the Lagrange multiplier. While the stiffness matrix K is singular, the augmented matrix in (A.2) is nonsingular and it yields the following solution. Left-multiplying the equation $K\boldsymbol{P} + c\boldsymbol{r} = \boldsymbol{F}$ by $\boldsymbol{r}^T$ implies that $c = (\boldsymbol{r}^T\boldsymbol{F})/(\boldsymbol{r}^T\boldsymbol{r})$, thus one has (the orthogonal projection) $K\boldsymbol{P} = \mathrm{proj}_{\mathcal{R}(K)}\boldsymbol{F}$, where $\mathcal{R}(K)$ is the range of K; and $\boldsymbol{r}^T\boldsymbol{P} = 0$ restricts that $\boldsymbol{P} \in \mathcal{R}(K)$.

Hence, the augmented system (A.1) addresses the two issues arising in solving the pressure Poisson equation: (i) it fixes the additive constant in p by choosing the zero-mean solution, and (ii) it ensures solvability, even when $\nabla \cdot \boldsymbol{u} = 0$ is violated (see Remark 2.1), by projecting the right hand side $\boldsymbol{F}$ to the range of K. Note that the augmented system (A.2) is similar to the one discussed in [33,35,42] where finite difference approaches are used.

References

[1] A. Krzywicki, O.A. Ladyzhenskaya, A grid method for the Navier-Stokes equations, Dokl. Akad. Nauk SSSR 167 (1966) 309–311.
[2] F.H. Harlow, J.E. Welch, Numerical calculation of time-dependent viscous incompressible flow of fluid with a free surface, Phys. Fluids 8 (1965) 2182–2189.
[3] M. Fortin, F. Brezzi, Mixed and hybrid finite element methods, Springer, New York, 1991.
[4] M. Benzi, G.H. Golub, J. Liesen, Numerical solution of saddle point problems, Acta Numer. 14 (2005) 1–137.
[5] C. Greif, T. Rees, D.B. Szyld, GMRES with multiple preconditioners, SeMA J. 74 (2017) 213–231.
[6] M. Benzi, M.A. Olshanskii, An augmented Lagrangian-based approach to the oseen problem, SIAM J. Sci. Comput. 28 (2006) 2095–2113.
[7] M. Benzi, M.A. Olshanskii, Field-of-values convergence analysis of augmented Lagrangian preconditioners for the linearized Navier-Stokes problem, SIAM J. Numer. Anal. 49 (2) (2011) 770–788.
[8] S. Le Borne, L.G. Rebholz, Preconditioning sparse grad-div/augmented Lagrangian stabilized saddle point systems, Comput. Vis. Sci. 16 (6) (2013) 259–269.
[9] S.C. Brenner, H. Li, L.-Y. Sung, Multigrid methods for saddle point problems: Stokes and Lamé systems, Numer. Math. 128 (2) (2014) 193–216.
[10] D.A. May, J. Brown, L. Le Pourhiet, A scalable, matrix-free multigrid preconditioner for finite element discretizations of heterogeneous Stokes flow, Comput. Methods Appl. Mech. Engrg. 290 (2015) 496–523.
[11] J. Rudi, G. Stadler, O. Ghattas, Weighted BFBT preconditioner for Stokes flow problems with highly heterogeneous viscosity, SIAM J. Sci. Comput. 39 (5) (2017).
[12] P.L. Lederer, A. Linke, C. Merdon, Schöberl, Divergence-free reconstruction operators for pressure-robust Stokes discretizations with continuous pressure finite elements, SIAM J. Numer. Anal. 55 (3) (2017) 1291–1314.
[13] P.W. Schroeder, G. Lube, Divergence-free H(div)-FEM for time-dependent incompressible flows with applications to high Reynolds number vortex dynamics, J. Sci. Comput. 72 (2) (2018) 830–858.
[14] P. Schroeder, V. John, P.L. Lederer, C. Lehrenfeld, G. Lube, J. Schöberl, On reference solutions and the sensitivity of the 2D Kelvin-Helmholtz instability problem, Comput. Math. Appl. 77 (4) (2019) 1010–1028.
[15] G. Lube, P.W. Schroeder, Implicit LES with high-order H(div)-conforming FEM for incompressible Navier-Stokes flows, 2018, arXiv: 1809.06558.
[16] T. Heister, G. Rapin, Efficient augmented Lagrangian-type preconditioning for the oseen problem using grad-div stabilization, Int. J. Numer. Methods Fluids 71 (2013) 118–134.
[17] D. Arndt, W. Bangerth, T.C. Clevenger, D. Davydov, M. Fehling, D. Garcia-Sanchez, G. Harper, T. Heister, L. Heltai, M. Kronbichler, R.M. Kynch, M. Maier, J.-P. Pelteret, B. Turcksin, W. D., The deal.II Library, Version 9.1, J. Numer. Math. 27 (2019) 203–213.
[18] A.J. Chorin, Numerical solution of the Navier-Stokes equations, Math. Comp. 22 (1968) 745–762.
[19] R. Temam, Sur l'approximation de la solution des équations de Navier-Stokes par la méthode des pas fractionnaries, II, Arch. Ration. Mech. Anal. 33 (3) (1969) 377–385.
[20] J.B. Perot, An analysis of the fractional step method, J. Comput. Phys. 108 (1993) 51–58.

[21] J.B. Bell, P. Colella, H. Glaz, A second-order projection method for the incompressible Navier-Stokes equations, J. Comput. Phys. 85 (2) (1989) 257–283.
[22] G.E. Karniadakis, M. Israeli, S. Orszag, High-order splitting methods for the incompressible Navier-Stokes equations, J. Comput. Phys. 97 (2) (1991) 414–443.
[23] J. Kim, P. Moin, Application of a fractional step method to incompressible Navier-Stokes equations, J. Comput. Phys. 59 (1985) 308–323.
[24] D.L. Brown, R. Cortez, M.L. Minion, Accurate projection methods for the incompressible Navier-Stokes equations, J. Comput. Phys. 168 (2) (2001) 464–499, http://dx.doi.org/10.1006/jcph.2001.6715, URL http://www.sciencedirect.com/science/article/pii/S0021999101967154.
[25] L. Rebholz, M. Xiao, Improved accuracy in algebraic splitting methods for Navier-Stokes equations, SIAM J. Sci. Comput. 39 (4) (2017) A1489–A1513.
[26] J.-G. Liu, J. Liu, R.L. Pego, Stable and accurate pressure approximation for unsteady incompressible viscous flow, J. Comput. Phys. 229 (9) (2010) 3428–3453.
[27] J.L. Guermond, P. Minev, J. Shen, An overview of projection methods for incompressible flows, Comput. Methods Appl. Mech. Eng. 195 (44–47) (2006) 6011–6045.
[28] M.L. Minion, R.I. Saye, Higher-order temporal integration for the incompressible Navier-Stokes equations in bounded domains, J. Comput. Phys. 375 (2018) 797–822.
[29] J. Stiller, A spectral deferred correction method for incompressible flow with variable viscosity, 2020, arXiv:2001.11902.
[30] J.L. Guermond, P. Minev, High-order time stepping for the incompressible Navier-Stokes equations, SIAM J. Sci. Comput. 37 (6) (2015) A2656–A2681, http://dx.doi.org/10.1137/140975231, arXiv:https://doi.org/10.1137/140975231.
[31] J.L. Guermond, P. Minev, High-order time stepping for the Navier-Stokes equations with minimal computational complexity, J. Comput. Appl. Math. 310 (2017) 92–103, http://dx.doi.org/10.1016/j.cam.2016.04.033, URL http://www.sciencedirect.com/science/article/pii/S0377042716302138.
[32] P.M. Gresho, R.L. Sani, On pressure boundary conditions for the incompressible Navier-Stokes equations, Internat. J. Numer. Methods Fluids 7 (1987) 1111–1145.
[33] W.D. Henshaw, A fourth-order accurate method for the incompressible Navier-Stokes equations on overlapping grids, J. Comput. Phys. 113 (6) (1994) 13–25.
[34] W.D. Henshaw, H.-O. Kreiss, L.G.M. Reyna, A fourth-order accurate difference approximation for the incompressible Navier-Stokes equations, Comput. Fluids 23 (4) (1994) 575–593.
[35] W.D. Henshaw, N.A. Petersson, A split-step scheme for the incompressible Navier-Stokes equations, in: M.M. Hafez (Ed.), Numerical Simulation of Incompressible Flows, Vol. 2502, World Scientific, 2003, pp. 108–125.
[36] N.A. Petersson, Stability of pressure boundary conditions for Stokes and Navier-Stokes equations, J. Comput. Phys. 172 (1) (2001) 40–70.
[37] H. Johnston, J.-G. Liu, A finite difference method for incompressible flow based on local pressure boundary conditions, J. Comput. Phys. 180 (1) (2002) 120–154.
[38] H. Johnston, J.-G. Liu, Accurate, stable and efficient Navier-Stokes solvers based on explicit treatment of the pressure term, J. Comput. Phys. 199 (1) (2004) 221–259.
[39] L. Kleiser, U. Schumann, Treatment of the incompressibility and boundary conditions in 3-D numerical spectral simulation of plane channel flows, in: E.H. Hirschel (Ed.), Notes on Numerical Fluid Mechanics, Proc. 3th GAMM Conf. on Numerical Methods in Fluid Mechanics, Vieweg, Braunschweig, 1980, pp. 165–173.
[40] D. Rempfer, On boundary conditions for the incompressible Navier-Stokes problems, Appl. Mech. Rev. 59 (3) (2006) 107–125.
[41] R. Sani, J. Shen, O. Pironneau, P. Gresho, Pressure boundary condition for the time-dependent incompressible Navier-Stokes equations, Internat. J. Numer. Methods Fluids 50 (6) (2006) 673–682.
[42] D. Shirokoff, R.R. Rosales, An efficient method for the incompressible Navier-Stokes equations on irregular domains with no-slip boundary conditions, high order up to the boundary, J. Comput. Phys. 230 (23) (2011) 8619–8646.
[43] Q. Zhang, GePUP: Generic projection and unconstrained PPE for fourth-order solutions of the incompressible Navier-Stokes equations with no-slip boundary conditions, J. Sci. Comput. 67 (3) (2016) 1134–1180, http://dx.doi.org/10.1007/s10915-015-0122-4.
[44] F. Meng, J.W. Banks, W.D. Henshaw, D.W. Schwendeman, Fourth-order accurate fractional-step IMEX schemes for the incompressible Navier-Stokes equations on moving overlapping grids, Comput. Methods Appl. Mech. Engrg. 366 (2020) 113040.
[45] L. Li, A split-step finite-element method for incompressible Navier-Stokes equations with high-order accuracy up-to the boundary, J. Comput. Phys. 408 (2020) 109274.
[46] W.D. Henshaw, H.-O. Kreiss, Analysis of a Difference Approximation for the Incompressible Navier-Stokes Equations, Tech. rep., Los Alamos National Laboratory, 1995.
[47] M. Ignatova, G. Iyer, J.P. Kelliher, R.L. Pego, A.D. Zarnescu, Global existence for two extended Navier-Stokes systems, 2013, arXiv preprint arXiv:1308.4735.
[48] D. Zhou, B. Seibold, D. Shirokoff, P. Chidyagwai, R.R. Rosales, Meshfree finite differences for vector Poisson and pressure Poisson equations with electric boundary conditions, in: M. Griebel, M.A. Schweitzer (Eds.), Meshfree Methods for Partial Differential Equations VII, in: Lecture Notes in Computational Science and Engineering, vol. 100, Springer, 2015, pp. 223–246.
[49] W. Layton, Introduction to the Numerical Analysis of Incompressible Viscous Flows, Society for Industrial and Applied Mathematics, Philadelphia, PA, USA, 2008.
[50] D.N. Arnold, R.S. Falk, J. Gopalakrishnan, Mixed finite element approximation of the vector Laplacian with Dirichlet boundary conditions, Math. Models Methods Appl. Sci. 22 (9) (2012) 1250024.

[51] D.N. Arnold, H. Chen, Finite element exterior calculus for parabolic problems, ESAIM Math. Model. Numer. Anal. 51 (1) (2017) 17–34, http://dx.doi.org/10.1051/m2an/2016013.
[52] D.N. Arnold, R.S. Falk, R. Winther, Finite element exterior calculus, homological techniques, and applications, Acta Numer. 15 (2006) 1–155.
[53] D.N. Arnold, R.S. Falk, R. Winther, Finite element exterior calculus: From hodge theory to numerical stability, Bull. Amer. Math. Soc. 47 (2) (2010) 281–354.
[54] I. Babuška, Stability of the domain with respect to the fundamental problems in the theory of partial differential equations, mainly in connection with the theory of elasticity, I, II, Czechoslovak Math. J. 11 (86) (1961) 76–105.
[55] I. Babuška, J. Pitkäranta, The plate paradox for hard and soft simple support, SIAM J. Math. Anal. 21 (3) (1990) 551–576.
[56] U. Kangro, R. Nicholaides, Divergence boundary conditions for vector Helmholtz equations with divergence constraints, ESAIM Math. Model. Numer. Anal. 33 (3) (1999) 479–492.
[57] U.M. Ascher, S.J. Ruuth, B. Wetton, Implicit-explicit methods for time-dependent partial differential equations, SIAM J. Numer. Anal. 32 (3) (1995) 797–823.
[58] U.M. Ascher, S.J. Ruuth, R.J. Spiteri, Implicit-explicit Runge-Kutta methods for time-dependent partial differential equations, Appl. Numer. Math. 25 (2) (1997) 151–167.
[59] J.C. Butcher, Coefficients for the study of Runge-Kutta integration processes, J. Aust. Math. Soc. 3 (02) (1963) 185–201.
[60] R.R. Rosales, B. Seibold, D. Shirokoff, D. Zhou, Unconditional stability for multistep ImEx schemes: Theory, SIAM J. Numer. Anal. 55 (5) (2017) 2336–2360, http://dx.doi.org/10.1137/16M1094324, arXiv:https://doi.org/10.1137/16M1094324.
[61] T. Koto, IMEX Runge-Kutta schemes for reaction-diffusion equations, J. Comput. Appl. Math. 215 (1) (2008) 182–195.
[62] D. Cavaglieri, T. Bewley, Low-storage implicit/explicit Runge-Kutta schemes for the simulation of stiff high-dimensional ODE systems, J. Comput. Phys. 286 (2015) 172–193, http://dx.doi.org/10.1016/j.jcp.2015.01.031, URL http://www.sciencedirect.com/science/article/pii/S0021999115000352.
[63] C.A. Kennedy, M.H. Carpenter, Additive Runge-Kutta schemes for convection-diffusion-reaction equations, Appl. Numer. Math. 44 (1) (2003) 139–181, http://dx.doi.org/10.1016/S0168-9274(02)00138-1, URL http://www.sciencedirect.com/science/article/pii/S0168927402001381.
[64] J.M. Sanz-Serna, J.G. Verwer, W.H. Hundsdorfer, Convergence and order reduction of runge-kutta schemes applied to evolutionary problems in partial differential equations, Numer. Math. 50 (4) (1986) 405–418.
[65] J.G. Verwer, Convergence and order reduction of diagonally implicit Runge-Kutta schemes in the method of lines, in: Numerical Analysis, 1986, pp. 220–237.
[66] M.H. Carpenter, D. Gottlieb, S. Abarbanel, W.-S. Don, The theoretical accuracy of Runge-Kutta time discretizations for the initial boundary value problem: a study of the boundary error, SIAM J. Sci. Comput. 16 (6) (1995) 1241–1252.
[67] R.R. Rosales, B. Seibold, D. Shirokoff, D. Zhou, Spatial manifestations of order reduction in Runge-Kutta methods for initial boundary value problems, 2019, arXiv preprint arXiv:1712.00897.
[68] I. Alonso-Mallo, Runge-kutta methods without order reduction for linear initial boundary value problems, Numer. Math. 91 (4) (2002) 577–603.
[69] D. Ketcheson, B. Seibold, D. Shirokoff, D. Zhou, DIRK schemes with high weak stage order, in: Lecture Notes in Computational Science and Engineering, Proceedings of ICOSAHOM 2018, Springer, 2020.
[70] B. Seibold, D. Shirokoff, D. Zhou, Unconditional stability for multistep ImEx schemes: Practice, J. Comput. Phys. 376 (2019) 295–321.
[71] A. Logg, K.-A. Mardal, G.N. Wells, et al., Automated Solution of Differential Equations by the Finite Element Method, Springer, Berlin, 2012, http://dx.doi.org/10.1007/978-3-642-23099-8.
[72] R.C. Kirby, Algorithm 839: FIAT, a new paradigm for computing finite element basis functions, ACM Trans. Math. Softw. 30 (4) (2004) 502–516, http://dx.doi.org/10.1145/1039813.1039820.
[73] R.C. Kirby, FIAT: Numerical construction of finite element basis functions, in: A. Logg, K.-A. Mardal, G.N. Wells (Eds.), Automated Solution of Differential Equations by the Finite Element Method, in: Lecture Notes in Computational Science and Engineering, vol. 84, Springer, Berlin, 2012, pp. 247–255, Ch. 13.
[74] C. Geuzaine, J.-F. Remacle, Gmsh: A 3-D finite element mesh generator with built-in pre-and post-processing facilities, Int. J. Numer. Methods Eng. 79 (11) (2009) 1309–1311.
[75] U. Ghia, K.N. Ghia, C.T. Shin, High-re solutions for incompressible flow using the Navier-Stokes equations and a multigrid method, J. Comput. Phys. 48 (3) (1982) 387–411, http://dx.doi.org/10.1016/0021-9991(82)90058-4, URL http://www.sciencedirect.com/science/article/pii/0021999182900584.
[76] E. Erturk, Numerical solution of 2-D steady incompressible flow over a backward-facing step, Part I: High Reynolds number solutions, Comput. & Fluids 37 (2008) 633–655.